Impact of SO_2 on NiFe Nanoparticle Exsolution and Dissolution from $LaFe_{0.9}Ni_{0.1}O_3$ Perovskite Oxides

Musa Najimu[a,b], Matthew J. Hurlock[c], Sahanaz Parvin[d], Courtney Brea[i], Neelesh Kumar[e], Yoon Jin Cho[j], Yiqing Wu Gao[f], Guoxiang Hu[i], Zili Wu[f,g], Eranda Nikolla[j], Jonas Baltrusaitis[d], Tina M. Nenoff[h], Israel E. Wachs[e], Kandis Leslie Gilliard-AbdulAziz[a,b]*

a. Department of Civil and Environmental Engineering, University of Southern California, Los Angeles, California 90089, United States

b. Department of Chemical and Environmental Engineering, University of California−Riverside, Riverside, California 92521, United States

c. Materials & Systems Design, Pacific Northwest National Laboratory, Richland, Washington 99345, United States

d. Department of Chemical and Biomolecular Engineering, Lehigh University, Bethlehem, Pennsylvania 18015, United States

e. Operando Molecular Spectroscopy and Catalysis Laboratory, Department of Chemical and Biomolecular Engineering, Lehigh University, Bethlehem, Pennsylvania 18015, United States

f. Chemical Sciences Division, Oak Ridge National Laboratory, Oak Ridge, Tennessee 37831, United States

g. Center for Nanophase Materials Sciences, Oak Ridge National Laboratory, Oak Ridge, Tennessee 37830, United States

h. Advanced Science and Technology, Sandia National Laboratories, Albuquerque, New Mexico 87185, United States

i. School of Materials Science and Engineering, College of Engineering, Georgia Institute of Technology, Atlanta, GA 30332, United States

j. Department of Chemical Engineering, University of Michigan, Ann Arbor, Michigan 48109, United States

*To whom all correspondence should be addressed. Telephone: (213) 821-2169.
E-mail address: kabdulaz@usc.edu

ABSTRACT

Ni-doped $LaFeO_3$ perovskite oxide is a promising cathode material for solid oxide electrolysis cells (SOECs) designed for CO_2/H_2O co-electrolysis. The performance of $LaFe_{0.9}Ni_{0.1}O_3$ is being investigated under real-world conditions that include exposure to acid gases like SO_2, relevant to SOEC operation. Experiments show that $LaFe_{0.9}Ni_{0.1}O_3$ exsolves NiFe nanoparticles, along with surface SO_4^{2-} and SO_3^{2-} after being exposed to 200 ppm of SO_2. This suggests that the ionic diffusion of Ni^{3+} and Fe^{3+} between the bulk and the surface remains unaffected throughout the exsolution-dissolution-exsolution cycle. Thermochemical water splitting has been employed as a probe reaction to evaluate the catalytic properties of the exsolved NiFe nanoparticles. These nanoparticles demonstrated improved hydrogen production compared to the bare perovskite oxide substrates. However, after exposure to SO_2, the formation of Fe-rich NiFe nanoparticles led to poor thermocatalytic performance and rapid deactivation of the perovskite at elevated temperatures. Density Functional Theory (DFT) analysis was utilized to validate the experimental findings, indicating a significantly negative reaction energy for water splitting over exsolved Fe, as well as stronger binding of SO_2 to Fe than to Ni. Computational analysis further suggests that the presence of surface sulfate promotes the formation of Fe-rich NiFe nanoparticles, aligning with the experimental results. Overall, this study clarifies how SO_2 affects the structure of SOEC perovskite oxide candidate materials. Future engineering efforts should focus on enhancing nanoparticle exsolution and sulfur resistance, which is crucial for improving the hydrogen production capacity of La-based perovskite oxides for electro- and thermocatalytic water splitting in real environments containing acid gases.

1. Introduction

Perovskite oxide materials (ABO_3) are emerging as an alternative to Ni/Yttria-stabilized zirconia (YSZ) for thermochemical and electrochemical energy conversion due to their excellent oxygen vacancy mobility, redox stability, and mixed ionic, protonic and electronic conductivity [1–4]. Perovskite oxides with mixed cation metals have superior oxygen vacancy formation and mobility compared to single cations [5,6]. This enhanced reducibility makes them well-suited for oxygen vacancy-promoted reactions like thermochemical and electrochemical water-splitting for hydrogen production and carbon utilization. The oxygen vacancy formation energy of perovskite oxides is lowered through B-site trivalent ions substitution and A-site substitution with alkali earth metal ions[7,8] which causes the distortion and weakening of metal-oxygen bond [9], resulting in enhanced reactivity for solid oxide electrolysis (SOEC) applications [10–13]. For SOEC applications, some families of perovskite oxides with the ability to exsolve catalyst nanoparticles such as Ni, Fe, Co, or any combination thereof can improve the performance of electrodes, particularly for the hydrogen evolution and carbon reduction reactions [4,14]. During exsolution, the reduction of the bulk powder facilitates the ionic diffusion of reducible B-cations to form nanoparticles strongly adhered to the surface [15,16]. The subsequent oxidation of the perovskite oxide promotes the nanoparticles to redissolve back into the bulk of the perovskite oxide precursor. This cyclic behavior between reducing and oxidizing atmospheres adds a dynamicity that can contribute to improving performance during harsh reaction conditions. However, while exsolved nanoparticles have improved stability compared to conventional catalyst systems, the repeated redox cycling of these systems under exposure to acid gases needs further investigation.

Anthropogenic sulfur pollutants, due to their oxidizing and acidic properties, are known to react with supported metal nanoparticles, leading to their poisoning and deactivation. The deposition of surface sulfur compounds, such as sulfite or sulfate species, can generally occur in metal nanoparticles after exposure to SO_2[17]. For example, Nickel-based catalysts after SO_2 exposure can form Ni-S layer, which can facilitate blockage and encapsulation of Ni-active sites [18]. However, the deactivation of active Ni catalysts due to sulfur poisoning can be prevented by alloying Ni with oxophilic metals such as Fe [19,20], Co [21] , and Ru [22] that act as a sacrificial metal. Anthropogenic SO_2 contamination significantly impacts the structure and catalytic performance of perovskite oxides, leading to sulfurization, phase transformations, and, in severe cases, complete structural degradation. [23,24].

Previous research has explored the impact of SO_2 contaminants on perovskite oxide-supported catalysts. For instance, a study examined the Ni and Co-supported $La_{0.75}Sr_{0.25}Cr_{0.5}Mn_{0.5}O_{3-\delta}$ (LSCrM) perovskite oxide phase [25]. The results showed that after 5 h of exposure to SO_2, the perovskite oxide lattice was destroyed, and X-ray diffraction (XRD) patterns indicated the formation of La_2O_2S, Sr_xS_y, Cr_xS_y, Ni sulfide, Co sulfide, and elemental sulfur. Additionally, even low concentrations of SO_2 in the air exposed to $La_xSr_{1-x}Co_{1-y}Fe_yO_3$ cathode material at 800°C can lead to the formation of $SrSO_4$, which blocks the electrochemically active region on the cathode material's surface[26]. Similarly, the phase of $La_{0.7}Sr_{0.3}CoO_3$ perovskite oxide undergoes total destruction after exposure to SO_2 and CO at 650°C, breaking down into oxide of Co, sulfide of Sr and La, and sulfite and sulfate species[23]. The structure of $LaCoO_3$ perovskite oxide completely decomposes after SO_2 exposure, forming $La_2(SO_4)_3$, $La_2(SO_3)_3$, $La_2O_2SO_4$, and CoO phases, with no trace of any remaining $LaCoO_3$ perovskite oxide structure [24]. Furthermore, while thermal treatment in high vacuum is ineffective for the regeneration of bulk sulfates in

poisoned $LaCoO_3$, a thermochemical reduction with H_2 provides a pathway for the regeneration of sulfated perovskite oxides.

Ni-doped $LaFeO_3$ undergoes a dynamic self-assembly process, where thermochemically active NiFe alloy exsolves from and reincorporates into the perovskite lattice[27,28]. This reversible behavior enhances its stability and reactivity, positioning it as a promising SOEC material for efficient clean hydrogen production. This article studies the influence of SO_2 exposure on the exsolution and catalytic activity of NiFe nanoparticles formed from $LaFe_{0.9}Ni_{0.1}O_3$ (LFNO) perovskite oxide as a potential electrode material in high-temperature SOECs operatable with SO_2-containing feedstocks. We are specifically interested in studying the intrinsic formation or exsolution of NiFe nanoparticles following SO_2 exposure and the utility of these nanoparticles for thermochemical water splitting. The formation and dissolution of exsolved nanoparticles were tracked using X-ray diffraction (XRD) and Scanning Transmission Electron Microscopy-Energy dispersive spectroscopy (STEM-EDS), while the surface and bulk dynamics of the perovskite oxide, before, during, and after exposure were tracked using in-situ Raman and in-situ Fourier Transform Infrared Spectroscopy (FTIR). Density Functional Theory calculations were performed to understand the formation of surface sulfur species and the SO_2 binding and water splitting on the exsolved NiFe nanoparticles.

2. Materials and Methods

2.1 Perovskite Oxide Powder Synthesis

$LaFe_{0.9}Ni_{0.1}O_3$ (LFNO) sample was prepared using the modified sol-gel pechini method [27,28] by dissolving an appropriate amount of $La(NO_3)_3.6H_2O$, $Fe(NO_3)_3.9H_2O$ and $Ni(NO_3)_2.6H_2O$ in water at 60^oC under stirring. Citric acid monohydrate (CA) and ethylene glycol butyl ether (EGBE) (mol ratio of the perovskite:CA:EGBE is 1:3:1) were dissolved in water, and the resulting solution

was added dropwise to the metal nitrate solution under stirring at 60°C for chelation of the metal ions. The mixture was continuously stirred at 60°C until gel was formed. The sample was then dried overnight in an oven at 110°C for NO_3^- and water removal. The resulting hydrogel was grinded and calcined in a muffle furnace at 800°C for two hours with an initial temperature ramping of 5°C/min to form the perovskite oxide structure. For reduction of the sample to generate exsolved nanoparticles, 50 mg of the sample was reduced in a quartz tube reactor (CATLAB) using 5% H_2/He with a temperature ramping at 10°C/min to 800°C and dwelling at this temperature for 2 h before cooling to room temperature in helium. For oxidation/reoxidation of the sample, the 50 mg of the catalyst is oxidized in the same quartz tube reactor using 20% O_2/He mixture while heating the sample at 10°C/min to 800°C, dwelling at this temperature for 2 h before cooling down in helium. Standard $LaFeO_3$ (LFO) and $LaNiO_3$ (LNO) perovskite oxide materials were prepared from $La(NO_3)_3.6H_2O$ and their respective $Fe(NO_3)_3.9H_2O$ and $Ni(NO_3)_2.6H_2O$ precursors using the same procedure as $LaFe_{0.9}Ni_{0.1}O_3$.

The nanostructured La_2NiO_4 (L2NO) sample was prepared via a reverse-microemulsion method similar to previous reports [29,30]. Two systems were separately prepared, each containing a precursor complex composed of cetyltrimethylammonium bromide (CTAB)/water/hexane/n-butanol (the mass ratio of CTAB to water is 1.6). The first microemulsion was prepared by dissolving $La(NO_3)_3 \cdot 6H_2O$ (99.999%, Sigma Aldrich) and $Ni(NO_3)_2 \cdot H_2O$ (99.999%, Sigma Aldrich) in deionized water. The second microemulsion was prepared by dissolving KOH (99.99%, Sigma Aldrich), which served as the precipitating agent, in deionized water. Both microemulsion systems were sonicated and stirred until homogeneity was achieved. Then, the microemulsion containing the precipitating agent was added to the system containing the metal nitrate salts. The final solution was stirred for 4 h. The resulting solution was centrifuged and

washed with ethanol and deionized water, followed by drying and calcination at 825°C for 2 h under argon to convert the precursor complex into oxide crystals.

2.2 SO_2 Exposure

The LFNO sample exposure was carried out at Oak Ridge National Laboratories. The sample was exposed to 200 ppm SO_2/He gas for 1 h, and then cooled down in He. Prior to the exposure, the sample temperature was first ramped up to 600^{o}C at 10^{o}C /min in He.

2.3 Materials Characterization

2.3.1 X-ray Diffraction (XRD) and Scanning Transmission Electron Microscopy (STEM)

X-ray diffraction (XRD) patterns of samples were collected using the PANalytical Empyrean series 2 that uses a Cu K-α radiation source. The spectra were collected with a step size of 0.013 ^{o} in a range of 2θ from 10^o to 80^o. Scanning Transmission Electron Microscopy (STEM) images of samples were collected on ThermoFisher Scientific (formerly FEI/Philips) Titan Themis 300, which was also used for EDS measurement. Prior to image collection, the powder sample was sonicated in DI water and deposited on the copper grid (Ted Pella, Redding CA) using a pipette, followed by coating with Au after drying the water off.

2.3.2 X-ray photoelectron spectroscopy (XPS) analysis

XPS analysis was performed using a SPECS instrument equipped with a μ-FOCUS 600 X-ray monochromator operating under UHV conditions. Al Kα radiation was used with an X-ray beam energy of 1486.7 eV and a power of 100 W. A PHOIBOS 1D-DLD hemispherical analyzer (0.85 eV energy resolution) was used to acquire the spectra. Survey spectra were acquired using a pass energy of 100 eV, a step size of 1 eV, and a dwell time of 100 ms. High-resolution scans were acquired using a pass energy of 20 eV, a step size of 0.1 eV, and a dwell time of 1 s. CasaXPS

2.3.23PR1.0 was used for data processing [31]. All spectra were calibrated to the C 1s peak at 285.0 eV. High-resolution XPS was used for the elemental composition analysis. The high-resolution XPS of each element was corrected using the Shirley background method [32]. The Scofield relative sensitivity factors (RSF) [33] were used in elemental quantification together with the instrument-measured transmission function and effective attenuation length correction (EAL) [34].

2.3.3 In situ Raman

Raman spectroscopy was conducted on a Horiba-Jobin Yvon LabRam-HR Evolution Raman spectrometer at Lehigh University, equipped with a 532 nm excitation wavelength laser source and a thermoelectrically cooled Horiba Synapse BIDD scientific CCD camera detector. The laser power was adjusted to 1.5 mW for all conditions to avoid sample degradation with a 50x objective (Olympus LMPlanFL N 50x, numerical aperture = 0.5), while the spectrometer was used with a 500 nm grating (600 grooves/mm) and a 100 μm hole, resulting in a spectral resolution of ~1.83 cm^{-1}. The 520.7 cm^{-1} band of a silicon wafer standard was used to calibrate the spectrometer prior to spectral acquisition. Powder catalysts were loaded into a YSZ padded reaction cell (Linkam CCR1000) and connected to a gas flow control system. A Linkam Temperature Controller (T95 HT System Controller) unit programmed the catalyst temperature, and a heating/cooling rate of 10°C min^{-1} was used throughout the in-situ experiments. Before each experiment, samples were dehydrated at 700 ^{0}C under 10% O_2/Ar (30 ml/min) and then cooled to 120^{o}C to acquire the Raman spectrum. Reduction of LFNO under Raman was conducted using 1% H_2/Ar while 10% O_2/Ar was used for oxidation, with temperature ramped at the rate of 10 ^{o}C/min incrementally from 120 ^{o}C to 700 ^{o}C and then cooled down to 120 ^{o}C. In situ Raman experiments are restricted to a reductive gas mixture of 1% H_2/Ar to prevent damage to the heating elements, which could occur at higher hydrogen concentrations. Consequently, this setup uses lower hydrogen levels than the reductive

treatment described in 2.3.1 for catalytic characterization. Despite this limitation, in situ Raman spectroscopy serves as a qualitative tool for monitoring changes in the bulk structure of the perovskite oxide parent material during exsolution. These analyses are conducted either prior to or following exposure to SO_2, offering valuable insights into the structural transformations under controlled experimental conditions.

2.3.4 Attenuated Transmission Reflectance-Fourier Transform Infrared Spectroscopy (ATR-FTIR) and In situ Fourier-transform infrared spectrometry (in situ - FTIR)

Attenuated Transmission Reflectance – Fourier Transform Infrared Spectroscopy (ATR-FTIR) spectra were collected on a ThermoFisher Scientific Nicolet iS50 FTIR Spectrometer in the University of California, Riverside Analytical Chemistry Instrumentation Facility. The spectrometer has a built-in diamond ATR crystal and a one-touch sampling operation with a resolution of 0.09 cm^{-1}. For spectra measurement, a small amount of solid powder sample was placed on the diamond crystal without any sample pretreatment or dehydration. Pressure was exerted with an anvil pressure tip to ensure good contact between the powder sample and the crystal. Prior to the first sample measurement, a background spectrum was collected and automatically subtracted for all sample spectra. In addition to the as-prepared LFNO sample, spectra were also collected for LFNO samples that had been exposed ex-situ to 200 ppm SO_2 at 600°C.

In situ, FTIR spectra were collected with a Fourier-transform infrared (FTIR) spectrometer (Thermo NICOLET 8700) (at Lehigh University) equipped with a high-sensitivity mercury-cadmium-telluride (MCT-A) detector and a Harrick Praying Mantis Attachment (Model DRA-2) for diffuse reflectance spectroscopy. Powder samples were loaded into a Harrick Scientific cell (HVC-DRP4) directly connected to a gas flow control system. A corrosion-resistant cell was used

for sulfur-adsorbate studies of ex-situ exposed LFNO samples. A Harrick ATC Temperature Controller unit controlled the reaction chamber's temperature. Ex-situ SO_2 exposed sample was exposed to 10% O_2/Ar and then subjected to temperature increase from RT to 500^{o}C, dwelling for 15 mins after every increase by 100 ^{o}C, before cooling down. For in-situ exposure of SO_2 to LFNO, firstly, the as-prepared LFNO sample was dehydrated at 500^{o}C under 10% O_2/Ar (30 ml/min), held for 1 hour, and then cooled down to 120^{o}C before spectrum acquisition. The sample was then exposed to 10% O_2/Ar or 5% H_2/Ar or Ar with the temperature ramp rate of 10^{o}C/min incrementally to 500^{o}C, where it dwells for 30 mins before cooling down to 120^{o}C for spectra acquisition.

2.3.5 Density functional theory (DFT) calculations

Spin-polarized DFT was performed using the Vienna *ab initio* simulation package (VASP) [35,36]. The electron exchange-correlation was represented by the functional of Perdew, Burke and Ernzerhof (PBE) of generalized gradient approximation (GGA) [37]. The ion-electron interaction was described using the projector-augmented wave (PAW) method [38]. The plane-wave cutoff was set to 400 eV, and a conjugate gradient method was applied to relax the geometry until interatomic forces were less than 0.025 eV/Å. The Brillouin zone was sampled using 3 x 3 x 1 Monkhorst-Pack k-point mesh. The adsorption energies of SO_2 and water-splitting reactants and products (i.e., H_2O, *OH, and *H) were calculated using, $\Delta E = E_{slab+ads} - E_{slab} - E_{ads}$ where $E_{slab+ads}$, E_{slab}, and E_{ads} are the energies of the LFNO slab with adsorbate(s), the LFNO slab, and the isolated adsorbate, respectively.

The LFNO (001) surface with the FeO termination was used to investigate the sulfate/sulfite formation and vibrational frequencies under a (de)hydrated environment. Surface species, including, bidentate sulfate and sulfite, monodentate sulfate and sulfite, and bisulfate,

were investigated. The LFNO perovskite was modeled with a 2 x 2 supercell with 7 atomic layers. The top three atomic layers, including adsorbates, were allowed to relax, while the bottom four atomic layers were fixed during optimization. Vacuum space in the z-direction is 20 Å to avoid unphysical interactions. Additional ionosorbed oxygen species were incorporated as O_2 is present under experimental conditions, interacting with SO_2 [39]. Explicit water molecules were included to capture the local environment of as-synthesized LFNO during IR spectroscopic measurements.

The exsolved nanoparticles were modeled with Ni/Fe nanoparticles supported by an LFNO substrate. The LFNO substrate was modeled with a 3 x 2 supercell with 4 atomic layers. The top two layers, including the nanoparticle and adsorbates, were allowed to relax, while the bottom two layers were fixed during geometry optimizations. Vacuum space of 20 Å was applied in the z-direction to avoid periodic interactions. The Ni/Fe nanoparticle is composed of three layers. The bottom layer has nine atoms, six atoms in the middle layer, and three atoms at the top layer with periodicity in the y-direction of the slab, generated by a cut of the Ni/Fe bulk cells, respectively, exposing (111) terminations [40,41]. We note that the nanoparticle only partly covers the LFNO substrate, allowing interactions of adsorbates at the nanoparticle-surface boundary to occur.

2.4 Water Splitting Experiments

The water splitting activity test was carried out in a quartz tube fixed bed microreactor (Hiden Analytical CATLAB, Warrington, United Kingdom) using a 50 mg catalyst sample. 5% H_2O/He continuously generated from the vapor generator is first flown in a bypass mode at 50 ml/min for 1.5 h for steam composition and flow stability. Switching to the analysis mode of the CATLAB, the stable flow of 5% H_2O/He is then passed over the perovskite oxide catalyst while the temperature is ramping to 600^0C, at which it remains for 1 h before ramping temperature down to room temperature under helium flow. The composition of the effluent gas from the microreactor

is measured using a Hiden quantitative gas analyzer (QGA) mass spectrometer, in which mass spectral responses were recorded for H_2O, H_2, He, and O_2. In the case of the SO_2-exposed LFNO sample, mass spectral responses of H_2S and SO_2 were additionally recorded during reduction, oxidation, and water-splitting reactions. $LaFe_{0.9}Ni_{0.1}O_3$ and its exsolved version before and after SO_2 exposure are characterized for their thermochemical water splitting activity capability to study the influence of SO_2 exposure on exsolution. The samples are subjected to the 5% H_2O/He exposure, ramping temperature to 600^{o}C at 10^{o}C/min and dwelling at 600^{o}C for 1 h.

3. Results and Discussion

3.1 Exsolution of NiFe Nanoparticles after Dry SO_2 Exposure

To study the influence of SO_2 on LFNO perovskite oxide and how it influences exsolution, as-prepared LFNO was exposed to SO_2 (200 ppm SO_2 in He gas) at 600^{o}C for 1 h, and the material properties and the exsolution-dissolution-exsolution cycle of the exposed LFNO were assessed. XPS analysis of the post sulfur exposure of the LFNO perovskite oxide material, shown in **Figure 1a,** shows binding energies at 167.5 eV and 169 eV for S $2p_{3/2}$ with their corresponding S $2p_{1/2}$, indicative of sulfite and sulfate, respectively [42]. As shown by the ATR-FTIR spectra in **Figure S1**, the intensity of a broad absorbance between 900-1300 cm^{-1} increases when the SO_2 exposure time is increased from 1 h to 4 h, while the as-prepared LFNO lacks the broad absorbance. The broad absorbance band is most likely composed of overlapping hydrated S-O bands[43–47] in which the frequencies of the absorption bands could have been modified by hydrogen bonding[48].

XRD of SO_2-exposed LFNO (**Figure 1b**) shows only the crystallographic planes of $LaFe_{0.9}Ni_{0.1}O_3$, with no noticeable transformation of the orthorhombic crystallographic structure of the $LaFe_{0.9}Ni_{0.1}O_3$ perovskite oxide material (**Figure 1b**), even after 4 h of SO_2 exposure **(Figure S2)**. In addition, the perovskite oxide material has no noticeable decomposition or

structural transformation [23,24,49]. Sulfate and sulfite species detected by XPS and FTIR have not been detected in XRD because the SO_2 does not influence the bulk structure. After hydrogen reduction of the SO_2-exposed LFNO, exsolved NiFe and Ni nanoparticles are formed in addition to the formation of La_2O_3, as indicated by the XRD patterns shown in **Figure 1b** [50,51]. When subsequently oxidized in 20% O_2/He, the exsolved NiFe nanoparticles redissolve entirely back into the perovskite oxide together with the disappearance of La_2O_3, regenerating the initial LFNO perovskite oxide structure (**Figure 1b**). The subsequent reduction leads to the re-exsolution and formation of the NiFe and Ni nanoparticles and the accompanying La_2O_3.

STEM-EDS images of SO_2-exposed LFNO in **Figure 2a** show a uniform distribution of Fe and Ni among La, with some sparingly dispersed sulfur. The EDS point compositional analysis, shown in **Table 1**, was used to measure the Fe/Ni ratio of the bulk or the exsolved NiFe nanoparticles. The average Fe/Ni for the bulk perovskite from SO_2-exposed LFNO had a ratio of 8.8, which is close to the measured nominal value of 9 for the pristine LFNO samples. **Figures 2b** and **2c** present STEM images of exsolved NiFe nanoparticles (NPs) from pristine LFNO and re-exsolved NiFe NPs from SO_2-exposed LFNO. The images reveal overlapping regions of Ni and Fe, as well as areas with dispersed Ni, indicating the formation of both NiFe and Ni nanoparticles. These observations align with the findings from the XRD analysis, further supporting the structural interpretation. Exsolved NiFe NPs from pristine LFNO have an average size of 55 ± 20 nm. However, the average size of exsolved NiFe NPs from SO_2-exposed LFNO decreases to an average size of 40 ± 8 nm with a lower particle density. The NiFe NPs from SO_2-exposed LFNO were oxidized in simulated air (20%O_2/He) and re-reduced (5%H_2/He) at 800 °C for 2 hrs to potentially regenerate the exsolved Ni and NiFe nanoparticles and remove sulfur adsorbate species. The average size of NiFe nanoparticles in the regenerated SO_2-exposed LFNO increased to 65 ± 16

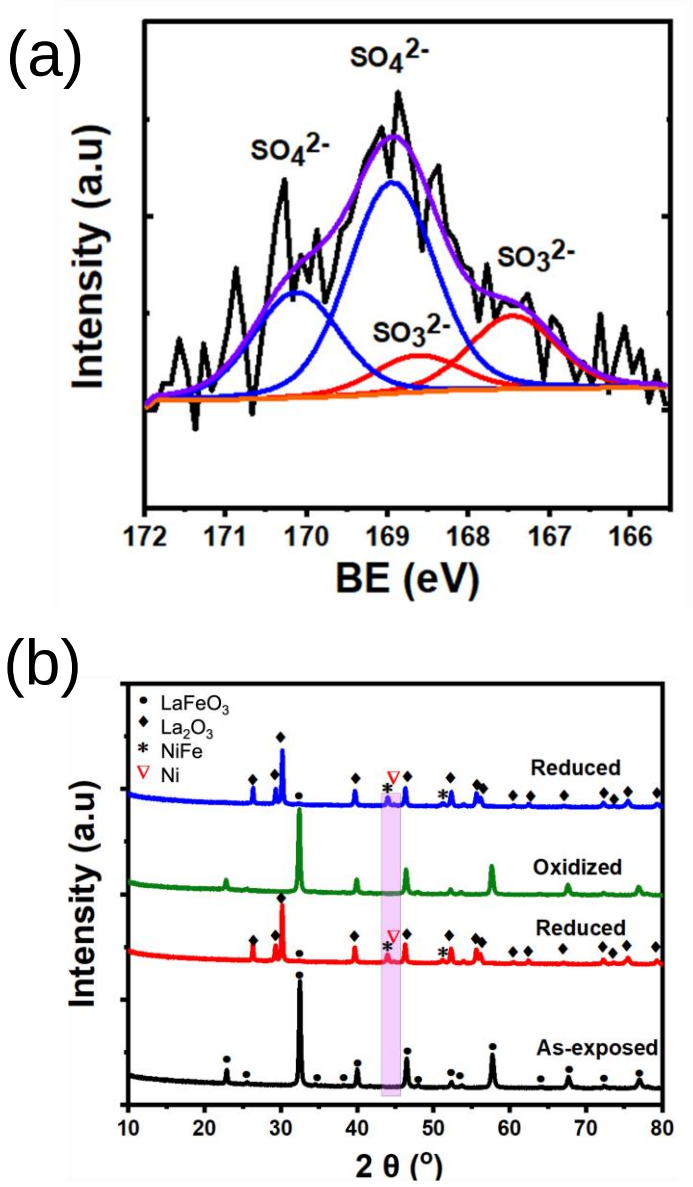

Figure 1: (a) S 2p XPS spectra of SO_2-exposed LFNO (200 ppm SO_2, 600°C for 1 h) (b) XRD of SO_2-exposed LFNO, reduced (SO_2-exposed), + oxidized (SO_2-exposed), + reduced (SO_2-exposed). Reduction: 5% H_2/He 800 °C for 2h, oxidation: 20% O_2/He 800 °C for 2 h

nm, accompanied by a further reduction in particle density. Additionally, the NiFe nanoparticles from the SO_2-exposed and regenerated materials exhibited a significant increase in Fe concentration. The average Fe/Ni ratio rose from 9.8 to 13.1 for the SO_2-exposed sample and to 13.9 for the regenerated sample, as detailed in **Table 1** and illustrated in **Figure S3**. The STEM-

EDS images (**Figure 2**) of the regenerated LFNO show sulfur species remain on the surface despite the high-temperature oxidative and reductive thermal treatments. Despite some formation of H_2S during reduction (see **Figure S5a**) and minimal SO_2 production during oxidation (see **Figure S5b**), we surmise that sulfur adsorbate species was only partially removed through hydrogen reduction.[47] Notably, despite the stable formation of sulfate and sulfite on the surface of LFNO, NiFe NPs can still be exsolved, dissolved, and re-exsolved. This suggests that SO_2 adsorbate species have minimal impact on the ionic transport of Ni and Fe from the bulk perovskite oxide to the surface. However, they significantly influence the composition of the exsolved metal nanoparticles, leading to an increased Fe content and the formation of more Fe-rich NiFe nanoparticles.

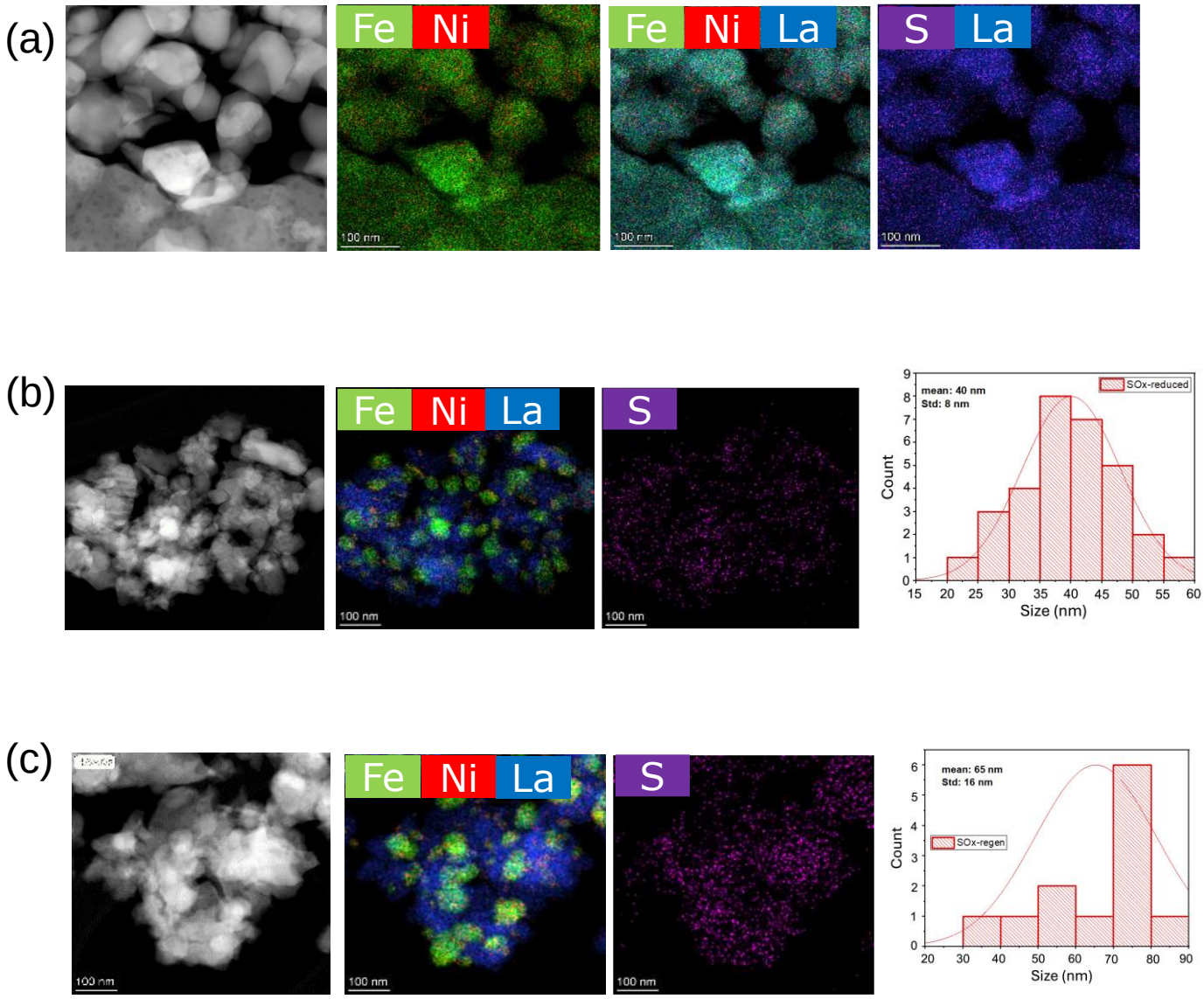

Figure 2: (a) STEM-EDS images of SO_2-exposed LFNO (b) STEM-EDS images and particle size distribution of reduced (SO_2-exposed) (c) STEM-EDS images and particle size distribution of regenerated (SO_2-exposed).

Table 1. EDS Compositional analysis of NiFe nanoparticle for Pristine NiFe/LFNO, NiFe/LFNO after SO_2-exposure, and regenerated NiFe/LFNO

Samples	Fe/Ni	Fe/Ni	Fe/Ni	Avg. Fe/Ni
Pristine NiFe/LFNO	9.5	8.9	11.0	9.8
NiFe/LFNO after SO_2-exposure to LFNO	15.1	12.0	12.1	13.1
NiFe/LFNO after Oxidative/reductive regeneration	16.7	12.4	12.7	13.9

3.2 Structural Changes in Bulk LFNO Perovskite Oxide Due to SO_2 Exposure

Raman spectroscopy was employed to investigate the bulk structural changes in LFNO during the exsolution of B-site metals, Ni and Fe. However, detecting low-frequency vibrations of exsolved metallic Ni/Fe nanoparticles proved challenging, so the focus was directed toward changes in the bulk perovskite oxide structure. **Figure S6** shows the Raman spectra of $LaFe_{0.9}Ni_{0.1}O_3$, $LaFeO_3$ (LFO), $LaNiO_3$ (LNO) and La_2NiO_4 (L2NO). The first-order vibrational bands in the spectral range of 100-700 cm^{-1} depict A-site modes (A), oxygen octahedral tilt (T), oxygen octahedral bending (B), or oxygen octahedral stretch (S) modes[52–54]. Specifically, the bands in the range of 450-700 cm^{-1} are for BO_6 octahedra internal vibration (stretch mode), which occurs at ~627 cm^{-1} and ~448 cm^{-1} for LFO and LNO, respectively. A new band at ~578 cm^{-1} in LFNO could be associated with the stretching mode in NiO_6 octahedra. Since this stretching mode is between the corresponding ~448 cm^{-1} (LNO) and ~627 cm^{-1} (LFO) modes, it can be concluded that Ni occupies the BO_6 octahedra in LFNO, thus confirming the doping of Ni at the B-sites of perosvkite oxide. The intensity of higher order vibrations (700-1350 cm^{-1}) reduced drastically in LFNO compared to LFO. Due to the structural disorder, defects, and crystallite size in the LFNO

after doping, the bands become broader compared to LFO and LNO. A slight blue shift in the bands of LFNO compared to LFO is due to the presence of Ni in the lattice, causing the strain in the unit cell, effectively distorting the structure by affecting FeO_6/NiO_6 octahedra and thus changing the Ni-O/Fe-O bond lengths. For $LaNiO_3$, bands at ~150, 197, 402, and 448 cm^{-1} are assigned to La vibrations, rotational/tilt mode, and vibrations of oxygen octahedra, respectively. The soft mode at ~197 cm^{-1} is of A_{1g} symmetry, reflecting the structural distortion to rhombohedral from cubic in LNO that scales with the octahedral tilt angle [55,56]. L2NO shows a spectrum with peaks at ~221 cm^{-1} and ~434 cm^{-1} assigned to E_g (La-O-Ni bending) and A_{1g} (La-O_2-Ni stretching) symmetry, respectively [57–59].

Figure 3a-c shows the in-situ Raman spectra of LFNO, LFO, and SO_2-exposed LFNO collected at 120 ^{0}C after the reduction and reoxidation treatments.. The reduction of LFNO at 700 ^{o}C and subsequent cooling to 120 ^{o}C under 1% H_2/Ar results in the enhanced intensity of the ~627 cm^{-1} band associated with Fe-O stretching compared to the ~578 cm^{-1} (Ni-O vibration) while a new band appears at ~1596 cm^{-1}. The dehydrated Raman spectrum of iron oxide as a reference is collected for the assignment of this new band. A peak in 1560-1600 cm^{-1} region appears close to ~1562 cm^{-1} which is due to the higher order vibrations (**Figure S6b**). Thus, ~1596 cm^{-1} band in the reduced LFNO is assigned to the higher order vibrational mode of FeOx species. The ~1596 cm^{-1} band appears during reduction at high temperature and persists after cooling to 120^{o}C under 1% H_2/Ar with an obvious blue shift due to thermal effects. The re-oxidation of the reduced LFNO at 700^{o}C and cooling to 120^{o}C under 10% O_2/Ar causes the 1596 cm^{-1} band disappearance, ultimately resulting in the Raman spectral features as of dehydrated LFNO at the start with similar relative intensity. The ~1596 cm^{-1} Raman band is not present in RP phase La_2NiO_4 (**Figure S6a**).The Raman spectra collected after the reduction of LFO under 1 % H_2/Ar at 700 ^{o}C and

cooling down to 120 ^{o}C shows an emerging additional band at ~1596 cm^{-1}, which also disappears after subsequent oxidation, while all the Raman modes of LFO remain intact (Figure 3b). This Raman band is posited to be a higher-order vibrations of FeOx species (**Figure S6b**). This could indicate the formation of $FeO_{x,}$ which is associated with the exsolution process of LFNO and LFO. FeOx nanoparticles were not detected by XRD or STEM-EDS measurements before or after exsolution. This lack of detection could indicate the low 1% H_2/Ar concentration used to induce exsolution for the Raman experiments as opposed to the 5%H_2/He used for the reactor-based regenerative studies. Thus, it can be concluded from the Raman studies that for LFNO, the vibrational band of at ~627 cm^{-1} for Fe-O stretching becomes slightly more enhanced after reduction suggesting exsolution of Ni from the host lattice. However, the disappearance of the exsolution-induced FeO_x after oxidation results in only Raman bands of dehydrated LFNO, which confirms the regenerability of the perovskite oxide material after exsolution. When directly subjected to oxidation with 10% O_2, both LFNO and LFO, demonstrate high thermal stability due to the lack of indication of any additional band although the characteristics Raman bands broaden due to thermal effects (**Figures S7 and Figure S8**). **Figure 3c** shows the Raman spectra of SO_2-exposed sample after reduction in 1 % H_2/Ar and oxidation in 10% O_2/Ar, in which the SO_2-exposed sample has been subjected to a maximum temperature of 500^{o}C due to the temperature limitation of the corrosion resistant properties of the in situ Raman cell used for this sample. After reduction at 500^{o}C, an-exsolution-induced FeO_x emerges with Raman band at ~1578 $cm^{-1,}$ which subsequently disappears after oxidation. The formation and disappearance of FeO_x species in the SO_2-exposed and pristine LFNO during reduction and oxidation, respectively, suggest that the exsolution mechanism of LFNO may not change after exposure to SO_2, indicating that the bulk structure of the LFNO perovskite oxide remains uninterrupted. Therefore, this suggests that the

LFNO perovskite oxide is structurally stable when exposed to SO_2 at 600°C and does not form bulk sulfate.

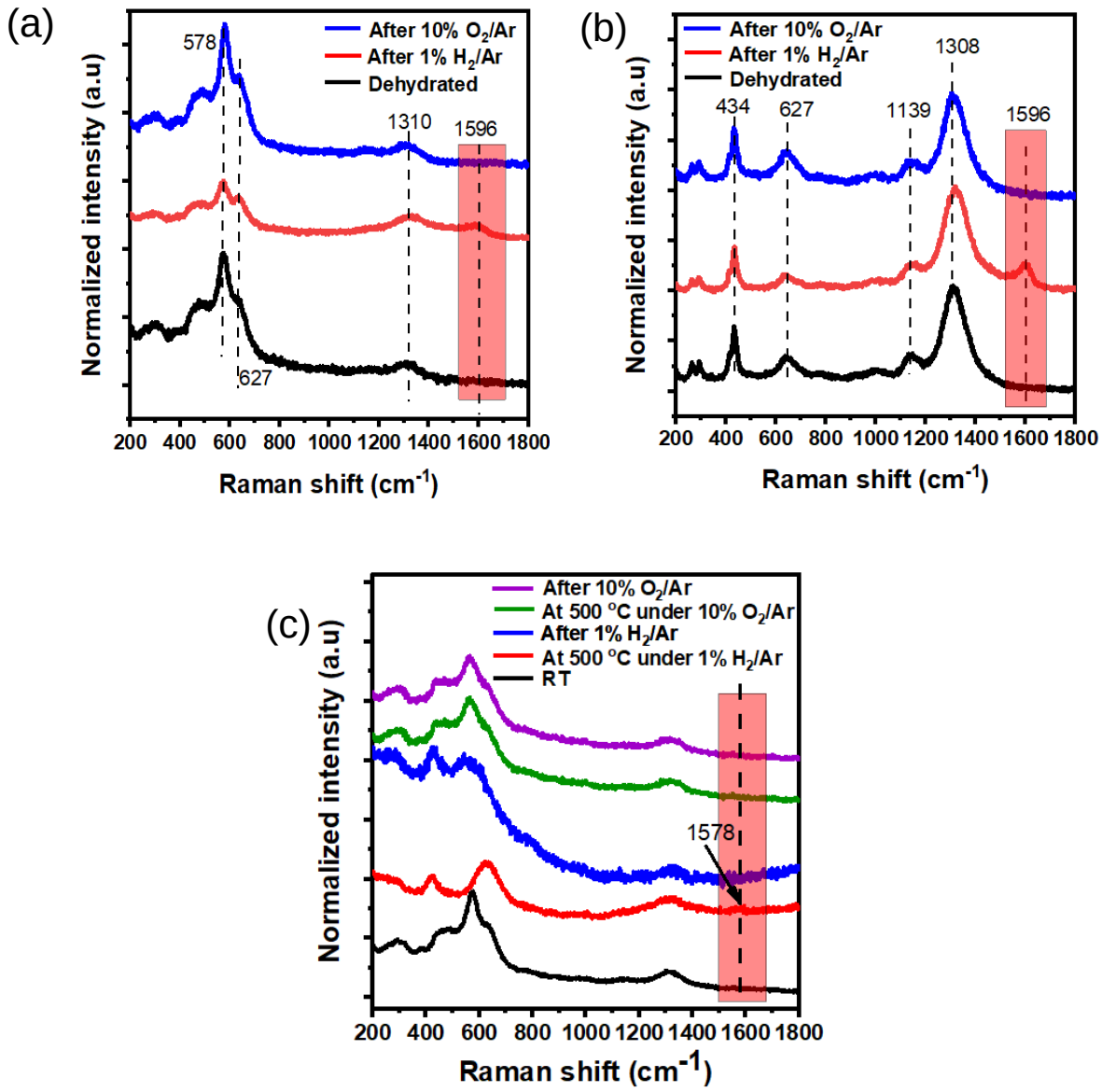

Figure 3: Raman spectra of (a) LFNO, (b) LFO after exposure to 1 % H_2/Ar at 700°C and cooling to 120°C; and subsequent exposure to 10% O_2/Ar at 700°C and cooling to 120°C. (c) SO_2-exposed LFNO; after exposure to 1% H_2/Ar at 500°C and cooling to 120°C; and subsequent exposure to 10% O_2/Ar at 500°C and cooling to 120°C.

3.3 Thermochemical Analysis of Water Splitting on SOEC Candidate Electrodes

Thermochemical water splitting was utilized as a probe reaction to examine the structural and compositional changes in the bulk perovskite oxide and the exsolved catalyst nanoparticles. As shown in **Figure 4a** and **Figure S9**, as-prepared LFNO demonstrates hydrogen production activity from thermochemical water splitting with an onset temperature of about 300°C. No oxygen was detected in the product stream, presumably, the oxygen is being consumed by the perovskite oxide lattice. Hydrogen production increases with increasing temperature, with a local maximum at about 390°C, reaching a relatively constant production after 600°C. Based on prior studies[10–12], oxygen vacancy in thermally reduced non-stoichiometric metal oxide and perovskite oxide materials are active for thermochemical water splitting. Compared to these studies, the oxygen vacancy of LFNO due to Ni incorporation could have been the primary active site for water splitting at a much lower temperature. The LFNO after exsolution of NiFe shows a hydrogen production onset temperature that is approximately 60°C lower than that of the as-prepared LFNO perovskite oxide and indicates a catalytic enhancement of the water-splitting activity. It also demonstrates a more enhanced local maximum hydrogen production at 400°C, and a sustained hydrogen production that is more than 3 times that of the as-prepared LFNO perovskite oxide at a constant temperature of 600°C (see **Figure 4a**). The improved hydrogen production is clearly attributed to the presence of the NiFe nanoparticles.

To understand the relevance of Ni and Fe in hydrogen production by the exsolved NiFe nanoparticles, Fe and Ni were exsolved from their respective $LaFeO_3$ and $LaNiO_3$ standard perovskite oxides for water splitting activity. Exsolved Fe/$LaFeO_3$ demonstrates hydrogen generation between 450-550°C, but the generation rapidly vanishes at higher temperatures (**Figure S10a**), most likely due to the rapid oxidation of Fe. On the other hand, hydrogen production by

exsolved Ni/$La(OH)_3$ begins at a lower temperature with a peak temperature between 250-400 ^oC and becomes sustained at higher temperatures (**Figure S10b**). The presence of Ni in exsolved NiFe enhances and maintains the water-splitting activity at elevated temperatures. Exsolved Ni/$La(OH)_3$ demonstrates a higher hydrogen production capacity than exsolved Fe/$LaFeO_3$. Both as-prepared standard $LaFeO_3$ and $LaNiO_3$ exhibit negligible water-splitting activity (**Figure S10a** and **Figure S10b**), possibly due to a lower concentration of oxygen vacancies.

For NiFe catalysts derived from SO_2-exposed LFNO, hydrogen production persists; however, the overall hydrogen production capacity of both the exsolved NiFe catalysts and the regenerated materials is significantly reduced compared to the pristine, as-prepared LFNO. Additionally, hydrogen production ceases entirely at 600°C, as shown in **Figures 4b** and **4c**. Similar to the NiFe/LFNO from pristine LFNO, NiFe/LFNO from the SO_2-exposed LFNO exhibits hydrogen production peak at temperatures between 250-400 and 450-550^oC, indicative of the formation of NiFe nanoparticles after SO_2 exposure. The overall reduction in hydrogen production capacity is attributed to a decline in the activity of both Ni and Fe during thermochemical water splitting following exposure to SO_2. This decline indicates a lower amount of active Ni and Fe remaining after exsolution, coupled with potential poisoning of active sites on the perovskite oxide support by residual sulfur adsorbate species. Although the exsolved NiFe nanoparticles are Fe-rich, as indicated by STEM-EDS, the hydrogen production capacity at ~500°C is relatively lower than at ~360°C. This reduction is due to a simultaneous decrease in the availability of active Ni and Fe, both of which are crucial contributors to hydrogen production at 500°C and higher temperatures. This can be attributed to the reduced NiFe nanoparticle density and increased particle size (**Figure S4** and **Figure 2**). Meanwhile, the exsolved NiFe and regenerated NiFe

samples after SO_2-exposure of LFNO demonstrate a lower temperature (~350^{o}C) of water splitting activity that indicates the influence of SO_2 on the nanoparticle formation.

The structural changes of the perovskite oxides were probed with XRD to determine any changes after exposure to water. As shown in the XRD patterns in **Figure S11a-b** and **Figure S12a-b**, there is no significant structural change in either standard $LaFeO_3$ or $LaNiO_3$ perovskite oxides after water exposure. Similar to as-prepared $LaFeO_3$ and $LaNiO_3$, no significant structural changes are detected in XRD after exposure of as-prepared LFNO to water (**Figure S13**), indicating some stability of the perovskite oxide to water exposure. Figure S15 presents the Raman spectra for LFNO, LFO, and SO_2-exposed LFNO under 10% H_2O. After heating all three samples to 700°C and cooling them to 120°C in the presence of water, the Raman bands of the samples remained unchanged from their initial state, with no new bands formed. This observation highlights the stability of these perovskite oxides under water exposure. As shown in the XRD patterns in **Figure S11a-b** and **Figure S12a-b,** reduced $LaFeO_3$ after water exposure, however, indicates segregation of Fe nanoparticles in an oxide form, and increased intensity of the $LaFeO_3$ XRD peak together with reduced La_2O_3 peak intensity could be indicative of partial reincorporation of some of the Fe atoms (**Figure S11**). Ni/$La(OH)_3$ obtained after the reduction of $LaNiO_3$ maintains its exsolved Ni after water exposure, and the original $LaNiO_3$ structure is not restored before reduction (**Figure S12**). The emergence of the La_2O_3 peak and intensity decrease of $La(OH)_3$ XRD peak after reduced $LaNiO_3$ water exposure suggests a transformation of some of $La(OH)_3$ to La_2O_3, possibly due to thermal dehydration[60] rather than $La(OH)_3$ decomposition that typically does not involve H_2 generation.. **Figure S14** compares the XRD patterns of the exsolved as-prepared, exsolved SO_2-exposed LFNO, and re-exsolved SO_2-exposed LFNO after the water-splitting reaction. For all three samples, water exposure causes the segregation of Fe from their

respective NiFe nanoparticles as Fe_3O_4, with a possible reincorporation of some Fe, similar to Fe segregation as Fe_3O_4 after water splitting over Fe/$LaFeO_3$.

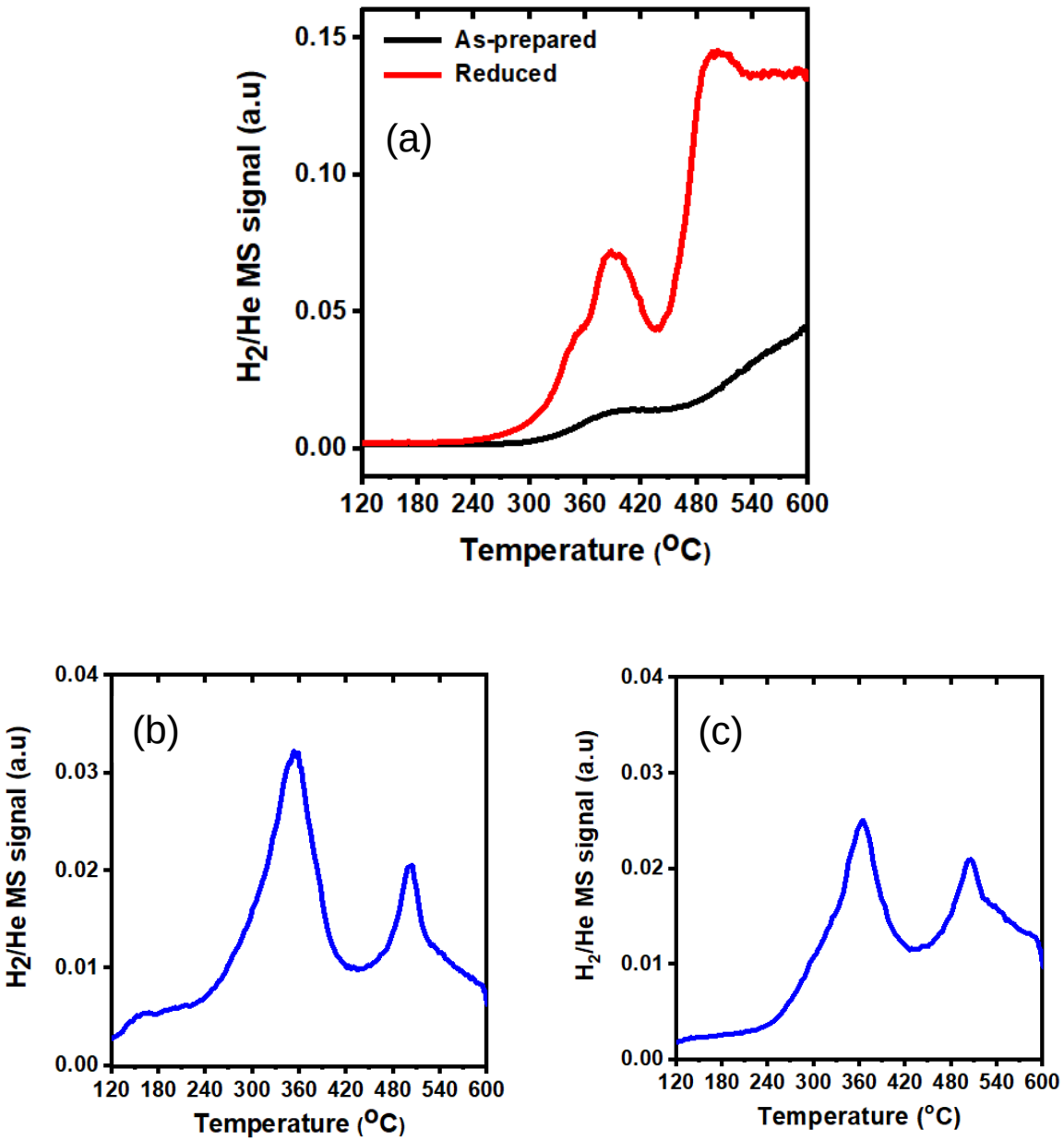

Figure 4: Normalized H_2 MS signal from water splitting performance of (a) as-prepared and reduced LFNO (b) reduced (SO_2-exposed) LFNO (c) regenerated -reoxidized and re-reduced (SO_2-exposed) LFNO [Water exposure: *5% H_2O/He, reduction: 5% H_2/He 800 ^oC for 2h, oxidation: 20% O_2/He 800 ^oC for 2 h]

3.4 Sulfur-Adsorbate Behavior under Environmental Conditions

The behavior of surface-adsorbed sulfur species on the LFNO perovskite oxide surface after SO_2 exposure is tracked under environmental conditions using in-situ Fourier Transform Infrared Spectroscopy (FTIR). **Figure 5a** shows the FTIR spectra of SO_2-exposed LFNO under an oxidative environment. A 990 cm^{-1} band is observed to increase slightly, suggesting a small amount of sulfate formation due to sulfite oxidation by the surface oxygen of LFNO or residual gas-phase oxygen. Decreasing intensities of 1137 and 1332 cm^{-1} can be considered as desorption or oxidation of weakly adsorbed SO_2 species since these vibrational frequencies are close to those of gas phase SO_2. The unchanged intensity of 981 and 1180 cm^{-1} bands can be assigned to other forms of sulfate species that are more thermally stable under an oxidative environment. However, bands at 1046, 1084, and 1105 decrease in intensities, suggesting interconversion of corresponding sulfur species, such as oxidation of sulfites to sulfate. Since there is no corresponding intensity enhancement of any of the S-O bands between 900-1300 cm^{-1} that could be attributed to sulfate species increment, the decreased intensity of the three bands could be due to desorption of sulfur species rather than due to sulfite species oxidation or due to effect of dehydration. For desorption, the sulfur species corresponding to the bands could still be sulfite species since they are generally less stable than sulfate species or monodentate sulfates rather than bidentate sulfates. In addition, an overall decrease in the total amount of adsorbed sulfur species suggests dehydration or thermal desorption as a predominant behavior of sulfur species under oxidation conditions. **Figure 5b** shows the in-situ FTIR spectra of exposed LFNO under Ar, which is very similar to the O_2/Ar spectra. Again, there is a significant decrease in the overall amount of adsorbed sulfur species based on the decreased band intensity. While a slightly increased intensity of 990 cm^{-1} can be due to sulfate species formation via sulfite oxidation by the surface lattice oxygen, unchanged bands

intensity at 981 cm^{-1} and 1180 cm^{-1} bands could denote thermally stable sulfate. Without a corresponding amount of sulfate formation, the decreasing intensities at 1046, 1084, and 1105 cm^{-1} in the inert Ar environment can be due to dehydration or due to thermal desorption of sulfites or monodentate even though SO_2 was not observed in the mass spectral analysis during oxidation of reduced SO_2-exposed LFNO possibly due its low concentration.

Due to the interference of desorption of sulfur species and their dehydration under Ar and O_2/Ar, the effect of oxidative and reducing environmental treatment conditions was considered on in-situ SO_2-exposed LFNO. **Figure 5c** shows the FTIR spectra of in-situ exposed LFNO before and after oxidation. In-situ SO_2 exposure of dehydrated LFNO indicates S-O bands at 986, 1048, 1137 and 1189 cm^{-1}. These bands match those of ex-situ SO_2 exposed LFNO after exposure to Ar or 10% O_2/Ar, indicating the dehydration effect of these two gas environments on the ex-situ SO_2-exposed LFNO rather than sulfur species desorption. The dehydration effect of Ar and O_2/Ar on ex-situ SO_2 exposed LFNO sample indicates that these bands are from surface-bound sulfur species rather than bulk sulfate. With Ar treatment of the in-situ exposed LFNO at 500^oC for 30 mins, the S-O bands remain expectedly unchanged. Similarly, oxidation with 10% O_2/Ar at 500^oC for 30 mins and reduction with 5 % H_2/Ar for 30 mins could not remove these bands. These indicate the high stability of these sulfur species under oxidizing and reducing environments. Based on DFT-calculated vibrational frequencies of (de)hydrated sulfur species on LFNO and

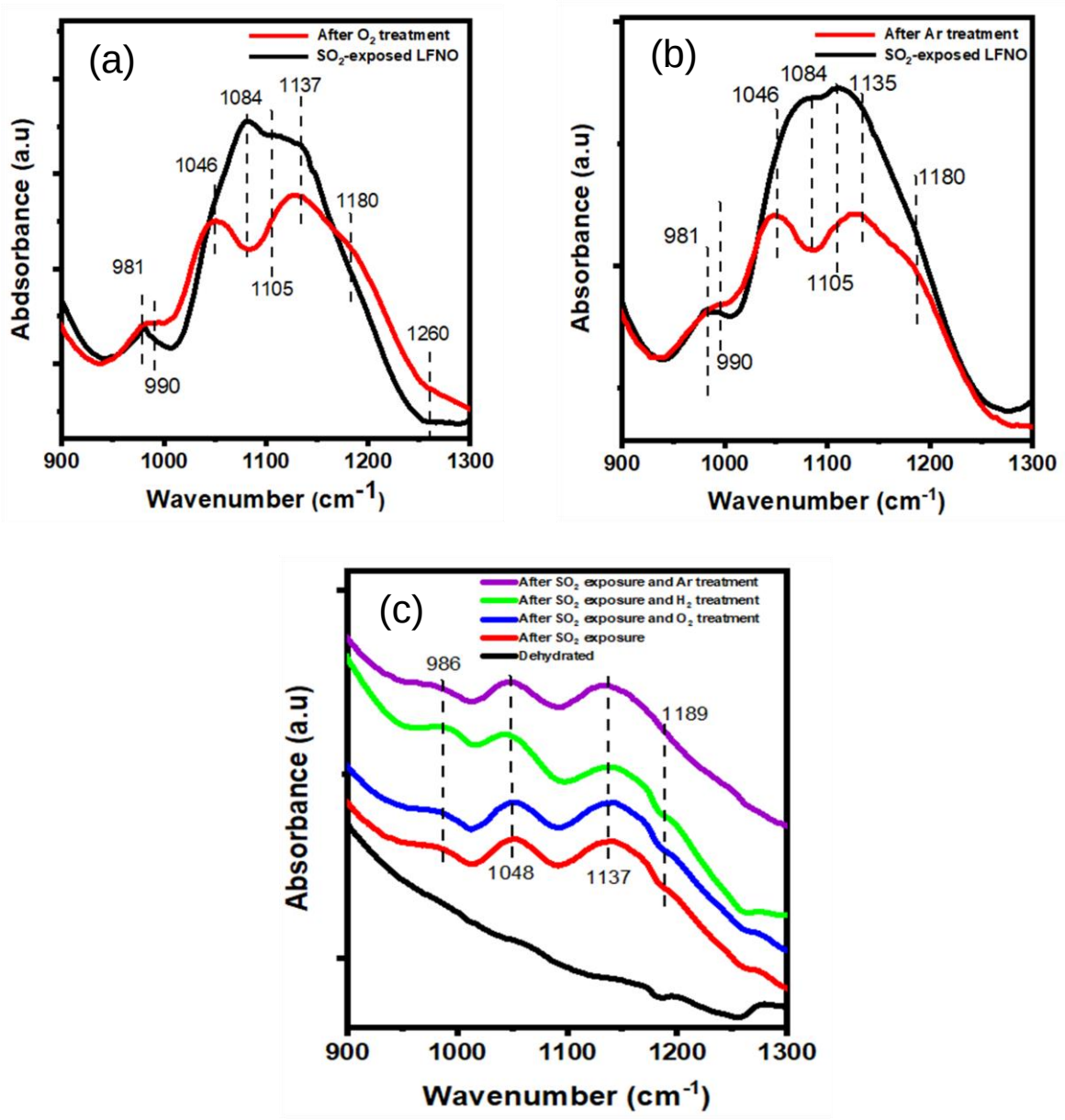

Figure *5*: In *situ* Fourier Transform Infrared Spectroscopy (FTIR) spectra of ex-situ SO_2-exposed LFNO (200 ppm SO_2 at 600ºC) under (a) 10% O_2/Ar and (b) Ar (c) In situ FTIR spectra of in-situ exposed LFNO (30 mins exposure to 200 ppm for 30 mins) followed by oxidation in 10% O_2/Ar for 30 mins or reduction in 5% H_2/Ar for 30 mins or Ar treatment for 30 mins.

LFO in **Figure S16, Figure S17** and **Table S1**, the experimentally observed 1084 cm^{-1} and 1105 cm^{-1} bands can be best assigned to bidentate sulfate and bisulfate respectively while bands around 990 cm^{-1} and 1135 cm^{-1} can be assigned to monodentate sulfite and bidentate sulfite respectively.

These findings indicate that during high-temperature exposure of LFNO to SO_2, the gas reacts with the perovskite oxide surface, leading to the formation of strongly bound mono- and bidentate sulfate and sulfite species. Even at 500°C, these surface sulfur species remain highly stable, resisting removal under both thermochemical reduction and oxidation conditions. The persistence of these sulfur species hinders the exsolution process by partially passivating active sites on the perovskite surface, thereby reducing the density of NiFe nanoparticles and potentially altering the catalytic performance of LFNO.

3.5 DFT Calculations of SO_2 Adsorption and Water-Splitting on LFNO

To understand the influence of SO_2 exposure on the composition of exsolved nanoparticles, we calculated the binding energy of SO_2 [61] on the exsolved nanoparticles. Various binding sites were considered, including the nanoparticle/LFNO interface, the exposed (111) surface of the nanoparticle, and the undercoordinated top site of the nanoparticle. We found that the energetically most favorable binding site for SO_2 is at the undercoordinated top sites of the exsolved nanoparticle. As shown in **Figure 6**, SO_2 is bound to Ni/Fe through two oxygen atoms in a bridged manner. The binding energy of SO_2 to the exsolved Ni and Fe was found to be -1.79 eV and -2.46 eV, respectively. The stronger/more favorable binding of SO_2 to the exsolved Fe NP suggests that exposure to SO_2 can provide a driving force toward the exsolution of more Fe to the surface under reducing/regenerative cycles. This agrees with STEM-EDS measurements shown in **Figure 2** and **Table 1** exhibiting Fe-rich nanoparticles after SO_2 exposure.

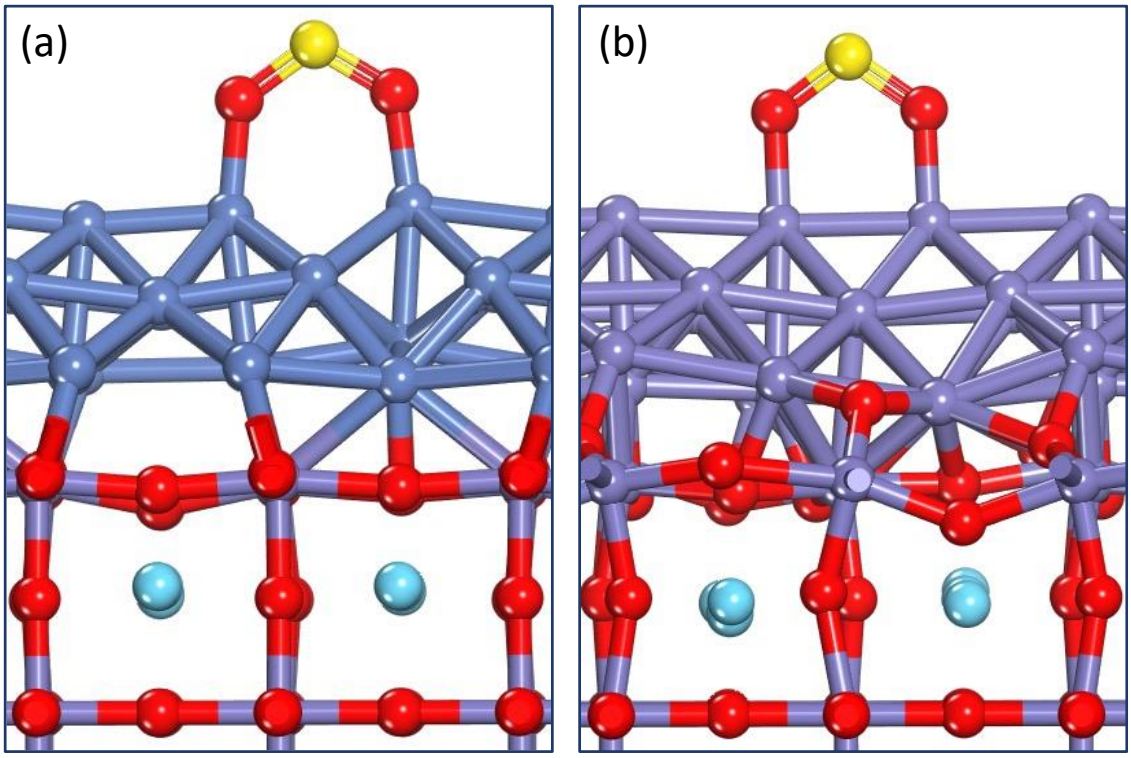

Figure 6: Optimized geometries of SO_2 at a) exsolved Ni nanoparticle top site and b) exsolved Fe nanoparticle top site. Ni, blue; Fe, light purple; O, red; La, cyan; S, yellow.

To gain insights into the catalytic mechanisms of water splitting on the exsolved nanoparticles, we compute the adsorption energy of water and the reaction energy of water splitting on the nanoparticles [62]. We found that the energetically most favorable adsorption site for H_2O is the undercoordinated top site for the exsolved Ni nanoparticle, while the exposed (111) surface for the exsolved Fe nanoparticle. As shown in **Figure 7**, in both cases, H_2O is bound to the nanoparticle through an oxygen atom. The binding energy of H_2O to the exsolved Ni and Fe was found to be -0.06 eV and -0.68 eV, respectively. Similar to SO_2, the exsolved Fe exhibits a stronger binding affinity to H_2O than the exsolved Ni. As for the water splitting, we found that the reaction

energy of H_2O dissociation to *OH and *H is -0.62 eV for the exsolved Ni, while -1.71 eV for the exsolved Fe. The facile dissociation of water (i.e., negative reaction energy) on both nanoparticles is in line with the experimentally observed enhanced catalytic activity of the reduced LFNO in comparison to the as-prepared LFNO (**Figure 4a**). The much more negative reaction energy of water splitting on the exsolved Fe explains the lower temperature of water splitting activity for the exsolved Fe-rich nanoparticles after SO_2 exposure (**Figure 4b**). However, the overly active Fe sites also suggest that the decrease in the catalytic activity at higher temperatures (~500^{o}C) could be attributed to the passivation/oxidation of the active sites.

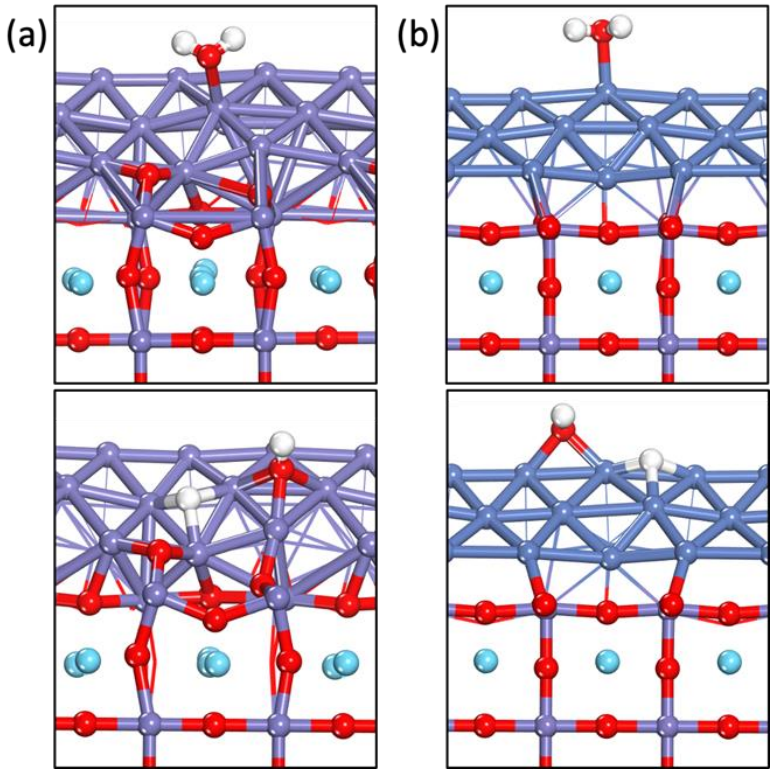

Figure 7: Optimized geometries of water splitting at exsolved Ni/Fe nanoparticle-LFO (a) H_2O and OH/H adsorption at Ni (111) (b) H_2O and OH/H adsorption at Fe (111). Ni, blue; Fe, light purple; O, red; La, cyan; H, white.

4. Conclusions

The influence of SO_2 exposure on the exsolution-dissolution cycle of perovskite oxides has been systematically investigated. XRD and STEM-EDS analyses reveal that the exsolution-dissolution-exsolution cycle can be sustained, but the exsolved nanoparticles exhibit increased Fe enrichment following SO_2 exposure. In-situ Raman spectroscopy indicates no significant structural changes in the bulk of the perovskite oxide before and after SO_2 exposure. Using a combination of ex-situ and in-situ FTIR, it was determined that SO_2 forms highly stable sulfate and sulfite species on the surface of LFNO perovskite oxide. These species demonstrate strong resistance to removal under both oxidizing and reducing conditions up to 500 °C. Interestingly, despite the formation of these stable surface species, NiFe alloy nanoparticles retain their ability to exsolve, dissolve, and re-exsolve, although the re-exsolved nanoparticles become more Fe-enriched, as confirmed by DFT studies. The exsolution of NiFe nanoparticles enhances the water-splitting performance of the perovskite oxide; however, this activity is diminished after SO_2 exposure. This reduction in activity is attributed to a lower density of exsolved nanoparticles and the increased Fe content in the NiFe nanoparticles. These findings provide critical insight into the deactivation mechanisms of LFNO perovskite oxide in high-temperature SO_2 environments. This understanding is essential for the design of robust perovskite oxide materials capable of directly utilizing coal power plant flue gas in solid oxide electrolysis cells.

Supporting Information.

XRD patterns of pristine and SOx-exposed LFNO and related materials, Raman spectra of structural changes of LFNO and related materials after exposure to water, STEM-EDS of LFNO and related materials before and after reduction, Select temperature-programmed surface reaction studies showing H_2 production via water splitting of LFNO samples and related materials, Optimized geometries and DFT calculated vibrational frequencies of (de)hydrated sulfur species on perovskite oxides.

ACKNOWLEDGMENT

This work was supported as part of UNCAGE-ME, an Energy Frontier Research Center funded by the United States Department of Energy, Office of Science, Basic Energy Sciences under Award DE-SC0012577. This article has been authored by an employee of National Technology & Engineering Solutions of Sandia, LLC under Contract No. DE-NA0003525 with the U.S. Department of Energy (DOE). The employee owns all right, title, and interest in and to the article and is solely responsible for its contents. The U.S. Government and the publisher, by accepting the article for publication, acknowledges that the U.S. Government retains a non-exclusive, paid-up, irrevocable, world-wide license to publish or reproduce the published form of this article or allow others to do so, for U.S. Government purposes. The DOE will provide public access to all results of federally sponsored research in accordance with the DOE Public Access Plan: https://www.energy.gov/downloads/doe-public-access-plan. This article has been authored by an employee of Pacific Northwest National Laboratory, a multiprogram national laboratory operated for the U.S. Department of Energy (DOE) by Battelle Memorial Institute under Contract No. DE-AC05-76RL01830.

AUTHOR INFORMATION

Corresponding author

Kandis Leslie Gilliard-AbdulAziz – Department of Chemical and Environmental Engineering, University of California Riverside

; Department of Civil and Environmental Engineering, University of Southern California

Authors

Musa Najimu – Department of Chemical and Environmental Engineering, University of California Riverside; Department of Civil and Environmental Engineering, University of Southern California

Matthew J. Hurlock – Materials & Systems Design, Pacific Northwest National Laboratory, Richland, Washington 99345, United States

Sahanaz Parvin – Department of Chemical and Biomolecular Engineering, Lehigh University, 111 Research Dr., Bethlehem, PA 18015, USA

Courtney Brea – School of Materials Science and Engineering, College of Engineering, Georgia Institute of Technology, 771 Ferst Dr NW, Atlanta, GA 30332, USA

Yoon Jin Cho – Department of Chemical Engineering, University of Michigan, Ann Arbor, MI, 48109

Yiqing Wu Gao – Chemical Sciences Division, Oak Ridge National Laboratory, Oak Ridge, Tennessee 37831, United States

Neelesh Kumar – Operando Molecular Spectroscopy and Catalysis Laboratory, Department of Chemical and Biomolecular Engineering, Lehigh University, Bethlehem, Pennsylvania 18015, United States

Guoxiang Hu – School of Materials Science and Engineering, College of Engineering, Georgia Institute of Technology, 771 Ferst Dr NW, Atlanta, GA 30332, USA

Zili Wu – Chemical Sciences Division, Oak Ridge National Laboratory, Oak Ridge, TN 37830, USA,
Center for Nanophase Materials Sciences, Oak Ridge National Laboratory, Oak Ridge, TN 37830, USA

Eranda Nikolla – Department of Chemical Engineering, University of Michigan, Ann Arbor, MI, 48109

Jonas Baltrusaitis – Department of Chemical and Biomolecular Engineering, Lehigh University, 111 Research Dr., Bethlehem, PA 18015, USA

Tina M. Nenoff – Advanced Science and Technology, Sandia National Laboratories, Albuquerque, New Mexico 87185, United States

Israel E. Wachs – Operando Molecular Spectroscopy and Catalysis Laboratory, Department of Chemical and Biomolecular Engineering, Lehigh University, Bethlehem, Pennsylvania 18015, United States

REFERENCES

(1) Teraoka, Y.; Zhang, H. M.; Okamoto, K.; Yamazoe, N. Mixed Ionic-Electronic Conductivity of La1− XSrxCo1− YFeyO3− δ Perovskite-Type Oxides. *Mater. Res. Bull.* **1988**, *23* (1), 51–58.

(2) Karczewski, J.; Bochentyn, B.; Molin, S.; Gazda, M.; Jasinski, P.; Kusz, B. Solid Oxide Fuel Cells with Ni-Infiltrated Perovskite Anode. *Solid State Ionics* **2012**, *221*, 11–14.

(3) Zhou, C.; Wang, X.; Liu, D.; Fei, M.; Dai, J.; Guan, D.; Hu, Z.; Zhang, L.; Wang, Y.; Wang, W. New Strategy for Boosting Cathodic Performance of Protonic Ceramic Fuel Cells through Incorporating a Superior Hydronation Second Phase. *Energy Environ. Mater.* **2024**, *7* (4), e12660.

(4) Ai, N.; Zou, Y.; Chen, Z.; Chen, K. Progress on Direct Assembly Approach for in Situ Fabrication of Electrodes of Reversible Solid Oxide Cells. *Mater. Reports Energy* **2021**, *1* (2), 100023.

(5) Wang, Y.; Zhou, J.; Chen, Z.; Zhuge, X.; Wang, Z. Tailoring Oxygen Vacancies by Synergy of Dual Metal Cations in LaCo0. 8M0. 2O3 (M= Cu, Ni, Fe, Mn) towards Catalytic Oxidation of Toluene. *J. Environ. Chem. Eng.* **2024**, 113555.

(6) Park, J.; Xu, B.; Pan, J.; Zhang, D.; Lany, S.; Liu, X.; Luo, J.; Qi, Y. Accurate Prediction of Oxygen Vacancy Concentration with Disordered A-Site Cations in High-Entropy Perovskite Oxides. *npj Comput. Mater.* **2023**, *9* (1), 29.

(7) Gokon, N.; Suda, T.; Kodama, T. Oxygen and Hydrogen Productivities and Repeatable Reactivity of 30-Mol%-Fe-, Co-, Ni-, Mn-Doped CeO2− δ for Thermochemical Two-Step Water-Splitting Cycle. *Energy* **2015**, *90*, 1280–1289.

(8) Dey, S.; Naidu, B. S.; Rao, C. N. R. Beneficial Effects of Substituting Trivalent Ions in

the B-Site of La 0.5 Sr 0.5 Mn 1− x A x O 3 (A= Al, Ga, Sc) on the Thermochemical Generation of CO and H 2 from CO 2 and H 2 O. *Dalt. Trans.* **2016**, *45* (6), 2430–2435.

(9) Chen, H.; Lim, C.; Zhou, M.; He, Z.; Sun, X.; Li, X.; Ye, Y.; Tan, T.; Zhang, H.; Yang, C. Activating Lattice Oxygen in Perovskite Oxide by B-site Cation Doping for Modulated Stability and Activity at Elevated Temperatures. *Adv. Sci.* **2021**, *8* (22), 2102713.

(10) Orfila, M.; Linares, M.; Molina, R.; Botas, J. Á.; Sanz, R.; Marugán, J. Perovskite Materials for Hydrogen Production by Thermochemical Water Splitting. *Int. J. Hydrogen Energy* **2016**, *41* (42), 19329–19338.

(11) Perez, A.; Orfila, M.; Linares, M.; Sanz, R.; Marugan, J.; Molina, R.; Botas, J. A. Hydrogen Production by Thermochemical Water Splitting with La0. 8Al0. 2MeO3-δ (Me= Fe, Co, Ni and Cu) Perovskites Prepared under Controlled PH. *Catal. Today* **2022**, *390*, 22–33.

(12) Wang, L.; Al-Mamun, M.; Zhong, Y. L.; Jiang, L.; Liu, P.; Wang, Y.; Yang, H. G.; Zhao, H. Ca 2+ and Ga 3+ Doped LaMnO 3 Perovskite as a Highly Efficient and Stable Catalyst for Two-Step Thermochemical Water Splitting. *Sustain. Energy Fuels* **2017**, *1* (5), 1013–1017.

(13) Xu, B.; Bhawe, Y.; Davis, M. E. Low-Temperature, Manganese Oxide-Based, Thermochemical Water Splitting Cycle. *Proc. Natl. Acad. Sci.* **2012**, *109* (24), 9260–9264.

(14) Xu, M.; Cao, R.; Qin, H.; Zhang, N.; Yan, W.; Liu, L.; Irvine, J. T. S.; Chen, D. Exsolved Materials for CO2 Reduction in High-Temperature Electrolysis Cells. *Mater. Reports Energy* **2023**, *3* (2), 100198.

(15) Najimu, M.; Jo, S.; Gilliard-AbdulAziz, K. L. Co-Exsolution of Ni-Based Alloy Catalysts

for the Valorization of Carbon Dioxide and Methane. *Acc. Chem. Res.* **2023**, *56* (22), 3132–3141.

(16) Shah, S.; Xu, M.; Pan, X.; Gilliard-Abdulaziz, K. L. Exsolution of Embedded Ni−Fe−Co Nanoparticles: Implications for Dry Reforming of Methane. *Cite This ACS Appl. Nano Mater* **2021**, *2021*, 8636. https://doi.org/10.1021/acsanm.1c02268.

(17) Rodriguez, J. A.; Jirsak, T.; Chaturvedi, S.; Hrbek, J.; Freitag, A.; Larese, J. Z. Chemistry of SO2 on Model Metal and Oxide Catalysts: Photoemission and XANES Studies. In *Studies in Surface Science and Catalysis*; Elsevier, 2000; Vol. 130, pp 3177–3182.

(18) Harris, W. M.; Lombardo, J. J.; Nelson, G. J.; Lai, B.; Wang, S.; Vila-Comamala, J.; Liu, M.; Liu, M.; Chiu, W. K. S. Three-Dimensional Microstructural Imaging of Sulfur Poisoning-Induced Degradation in a Ni-YSZ Anode of Solid Oxide Fuel Cells. *Sci. Rep.* **2014**, *4* (1), 5246.

(19) Papaioannou, E. I.; Neagu, D.; Ramli, W. K. W.; Irvine, J. T. S.; Metcalfe, I. S. Sulfur-Tolerant, Exsolved Fe–Ni Alloy Nanoparticles for CO Oxidation. *Top. Catal.* **2019**, *62*, 1149–1156.

(20) Steiger, P.; Burnat, D.; Kröcher, O.; Heel, A.; Ferri, D. Segregation of Nickel/Iron Bimetallic Particles from Lanthanum Doped Strontium Titanates to Improve Sulfur Stability of Solid Oxide Fuel Cell Anodes. *Catalysts* **2019**, *9* (4), 332.

(21) Jiang, C.; Loisel, E.; Cullen, D. A.; Dorman, J. A.; Dooley, K. M. On the Enhanced Sulfur and Coking Tolerance of Ni-Co-Rare Earth Oxide Catalysts for the Dry Reforming of Methane. *J. Catal.* **2021**, *393*, 215–229.

(22) Yuan, C.; Yao, N.; Wang, X.; Wang, J.; Lv, D.; Li, X. The SiO2 Supported Bimetallic Ni–Ru Particles: A Good Sulfur-Tolerant Catalyst for Methanation Reaction. *Chem. Eng. J.*

2015, *260*, 1–10.

(23) Hibbert, D. B. Reduction of Sulfur Dioxide on Perovskite Oxides. *Catal. Rev.* **1992**, *34* (4), 391–408.

(24) Zhu, Y.; Tan, R.; Feng, J.; Ji, S.; Cao, L. The Reaction and Poisoning Mechanism of SO2 and Perovskite LaCoO3 Film Model Catalysts. *Appl. Catal. A Gen.* **2001**, *209* (1–2), 71–77.

(25) Li, Y.; Na, L.; Lü, Z.; Li, S. Sulfur Poisoning and the Regeneration of the Solid Oxide Fuel Cell with Metal Catalyst-Impregnated La0. 75Sr0. 25Cr0. 5Mn0. 5O3-δ Anode. *Int. J. Hydrogen Energy* **2020**, *45* (31), 15650–15657.

(26) Wang, F.; Yamaji, K.; Cho, D.-H.; Shimonosono, T.; Kishimoto, H.; Brito, M. E.; Horita, T.; Yokokawa, H. Effect of Strontium Concentration on Sulfur Poisoning of LSCF Cathodes. *Solid State Ionics* **2012**, *225*, 157–160.

(27) Shah, S.; Hong, J.; Cruz, L.; Wasantwisut, S.; Bare, S. R.; Gilliard-AbdulAziz, K. L. Dynamic Tracking of NiFe Smart Catalysts Using In Situ X-Ray Absorption Spectroscopy for the Dry Methane Reforming Reaction. *ACS Catal.* **2023**, *13* (6), 3990–4002.

(28) Shah, S.; Sayono, S.; Ynzunza, J.; Pan, R.; Xu, M.; Pan, X.; Gilliard-AbdulAziz, K. L. The Effects of Stoichiometry on the Properties of Exsolved Ni-Fe Alloy Nanoparticles for Dry Methane Reforming. *AIChE J.* **2020**, *66* (12), e17078.

(29) Carneiro, J. S. A.; Brocca, R. A.; Lucena, M. L. R. S.; Nikolla, E. Optimizing Cathode Materials for Intermediate-Temperature Solid Oxide Fuel Cells (SOFCs): Oxygen Reduction on Nanostructured Lanthanum Nickelate Oxides. *Appl. Catal. B Environ.* **2017**, *200*, 106–113.

(30) Carneiro, J. S. A.; Williams, J.; Gryko, A.; Herrera, L. P.; Nikolla, E. Embracing the

Complexity of Catalytic Structures: A Viewpoint on the Synthesis of Nonstoichiometric Mixed Metal Oxides for Catalysis. *ACS Catalysis*. ACS Publications 2019, pp 516–527.

(31) Fairley, N.; Fernandez, V.; Richard-Plouet, M.; Guillot-Deudon, C.; Walton, J.; Smith, E.; Flahaut, D.; Greiner, M.; Biesinger, M.; Tougaard, S. Systematic and Collaborative Approach to Problem Solving Using X-Ray Photoelectron Spectroscopy. *Appl. Surf. Sci. Adv.* **2021**, *5*, 100112.

(32) Shirley, D. A. High-Resolution X-Ray Photoemission Spectrum of the Valence Bands of Gold. *Phys. Rev. B* **1972**, *5* (12), 4709.

(33) Scofield, J. H. Hartree-Slater Subshell Photoionization Cross-Sections at 1254 and 1487 EV. *J. Electron Spectros. Relat. Phenomena* **1976**, *8* (2), 129–137.

(34) Seah, M. P. Simple Universal Curve for the Energy-dependent Electron Attenuation Length for All Materials. *Surf. interface Anal.* **2012**, *44* (10), 1353–1359.

(35) Kresse, G.; Furthmüller, J. Efficiency of Ab-Initio Total Energy Calculations for Metals and Semiconductors Using a Plane-Wave Basis Set. *Comput. Mater. Sci.* **1996**, *6* (1), 15–50.

(36) Kresse, G.; Furthmüller, J. Efficient Iterative Schemes for Ab Initio Total-Energy Calculations Using a Plane-Wave Basis Set. *Phys. Rev. B* **1996**, *54* (16), 11169.

(37) Perdew, J. P.; Burke, K.; Ernzerhof, M. Generalized Gradient Approximation Made Simple. *Phys. Rev. Lett.* **1996**, *77* (18), 3865.

(38) Blöchl, P. E. Projector Augmented-Wave Method. *Phys. Rev. B* **1994**, *50* (24), 17953.

(39) Queralto, A.; Graf, D.; Frohnhoven, R.; Fischer, T.; Vanrompay, H.; Bals, S.; Bartasyte, A.; Mathur, S. LaFeO3 Nanofibers for High Detection of Sulfur-Containing Gases. *ACS Sustain. Chem. Eng.* **2019**, *7* (6), 6023–6032.

(40) Shishkin, M.; Ziegler, T. Oxidation of H2, CH4, and CO Molecules at the Interface between Nickel and Yttria-Stabilized Zirconia: A Theoretical Study Based on DFT. *J. Phys. Chem. C* **2009**, *113* (52), 21667–21678.

(41) Shishkin, M.; Ziegler, T. Direct Modeling of the Electrochemistry in the Three-Phase Boundary of Solid Oxide Fuel Cell Anodes by Density Functional Theory: A Critical Overview. *Phys. Chem. Chem. Phys.* **2014**, *16* (5), 1798–1808.

(42) Andreu, N.; Flahaut, D.; Dedryvère, R.; Minvielle, M.; Martinez, H.; Gonbeau, D. XPS Investigation of Surface Reactivity of Electrode Materials: Effect of the Transition Metal. *ACS Appl. Mater. Interfaces* **2015**, *7* (12), 6629–6636.

(43) Le, N. T. N.; Le, N. T. T.; Nguyen, Q. L.; Pham, T. L.-B.; Nguyen-Le, M.-T.; Nguyen, D. H. A Facile Synthesis Process and Evaluations of α-Calcium Sulfate Hemihydrate for Bone Substitute. *Materials (Basel).* **2020**, *13* (14), 3099.

(44) Kadam, S. S.; Mesbah, A.; Van der Windt, E.; Kramer, H. J. M. Rapid Online Calibration for ATR-FTIR Spectroscopy during Batch Crystallization of Ammonium Sulphate in a Semi-Industrial Scale Crystallizer. *Chem. Eng. Res. Des.* **2011**, *89* (7), 995–1005.

(45) Das, G.; Kakati, N.; Lee, S. H.; Karak, N.; Yoon, Y. S. Water Soluble Sodium Sulfate Nanorods as a Versatile Template for the Designing of Copper Sulfide Nanotubes. *J. Nanosci. Nanotechnol.* **2014**, *14* (6), 4455–4461.

(46) Arora, M.; Pradhan, M. M.; Bansal, M. C. Study of Vibrational Spectra of Lanthanum Sulphate Nonahydrate at Different Temperatures in the Region from 4000–50 Cm− 1. *Infrared Phys.* **1993**, *34* (6), 595–600.

(47) Zhang, R.; Alamdari, H.; Kaliaguine, S. SO2 Poisoning of LaFe0. 8Cu0. 2O3 Perovskite Prepared by Reactive Grinding during NO Reduction by C3H6. *Appl. Catal. A Gen.* **2008**,

340 (1), 140–151.

(48) Liu, Y.; Wang, A.; Freemen, J. J. Raman, MIR, and NIR Spectroscopic Study of Calcium Sulfates: Gypsum, Bassanite, and Anhydrite. In *40th Annual Lunar and Planetary Science Conference*; 2009; p 2128.

(49) Budiman, R. A.; Liu, S. S.; Bagarinao, K. D.; Ishiyama, T.; Kishimoto, H.; Yamaji, K.; Horita, T.; Yokokawa, H. Determination of Factors Governing Surface Composition and Degradation of La0. 6Sr0. 4Co0. 2Fe0. 8O3-δ Electrode under Sulfur-Contained Air. *J. Electrochem. Soc.* **2019**, *166* (6), F414.

(50) Singh, A.; Palakollu, V.; Pandey, A.; Kanvah, S.; Sharma, S. Green Synthesis of 1, 4-Benzodiazepines over La 2 O 3 and La (OH) 3 Catalysts: Possibility of Langmuir–Hinshelwood Adsorption. *RSC Adv.* **2016**, *6* (105), 103455–103462.

(51) Qazi, U. Y.; Yuan, C.-Z.; Ullah, N.; Jiang, Y.-F.; Imran, M.; Zeb, A.; Zhao, S.-J.; Javaid, R.; Xu, A.-W. One-Step Growth of Iron–Nickel Bimetallic Nanoparticles on FeNi Alloy Foils: Highly Efficient Advanced Electrodes for the Oxygen Evolution Reaction. *ACS Appl. Mater. Interfaces* **2017**, *9* (34), 28627–28634.

(52) Paul Blessington Selvadurai, A.; Pazhanivelu, V.; Jagadeeshwaran, C.; Murugaraj, R.; Mohammed Gazzali, P. M.; Chandrasekaran, G. An Analysis on Structural and Magnetic Properties of La 1− x RE x FeO 3 (X= 0.0 and 0.5, RE= Nd, Sm and Gd) Nanoparticles. *Appl. Phys. A* **2017**, *123*, 1–11.

(53) Weber, M. C.; Guennou, M.; Zhao, H. J.; Íñiguez, J.; Vilarinho, R.; Almeida, A.; Moreira, J. A.; Kreisel, J. Raman Spectroscopy of Rare-Earth Orthoferrites R FeO 3 (R= La, Sm, Eu, Gd, Tb, Dy). *Phys. Rev. B* **2016**, *94* (21), 214103.

(54) Lakshmi, R. V; Bera, P.; Hiremath, M.; Dubey, V.; Kundu, A. K.; Barshilia, H. C.

Structural, Magnetic, and Dielectric Properties of Solution Combustion Synthesized LaFeO 3, LaFe 0.9 Mn 0.1 O 3, and LaMnO 3 Perovskites. *Phys. Chem. Chem. Phys.* **2022**, *24* (9), 5462–5478.

(55) Chaban, N.; Weber, M.; Pignard, S.; Kreisel, J. Phonon Raman Scattering of Perovskite LaNiO3 Thin Films. *Appl. Phys. Lett.* **2010**, *97* (3), 031915.

(56) Abrashev, M. V; Litvinchuk, A. P.; Iliev, M. N.; Meng, R. L.; Popov, V. N.; Ivanov, V. G.; Chakalov, R. A.; Thomsen, C. Comparative Study of Optical Phonons in the Rhombohedrally Distorted Perovskites LaAlO 3 and LaMnO 3. *Phys. Rev. B* **1999**, *59* (6), 4146.

(57) De Andres, A.; Fernandez-Diaz, M. T.; Martinez, J. L.; Rodriguez-Carvajal, J.; Saez-Puche, R.; Fernandez, F. Raman Scattering of Orthorhombic and Tetragonal Ln2NiO4+ Delta (Ln Identical to La, Pr, Nd) Oxides. *J. Phys. Condens. Matter* **1991**, *3* (21), 3813.

(58) Udagawa, M.; Yamaguchi, T.; Nagaoka, Y.; Ogita, N.; Kato, M.; Maeno, Y.; Fujita, T.; Ohbayashi, K. Phonon Raman Scattering of (La 1− x Sr x) 2 NiO 4. *Phys. Rev. B* **1993**, *47* (17), 11391.

(59) Bates, F. E.; Eldridge, J. E. Normal Modes of Tetragonal La2NiO4 and La2CuO4, Isomorphs of the Hight Tc Superconductor La2-XSrxCuO4. *Solid State Commun.* **1989**, *72* (2), 187–190.

(60) Neumann, A.; Walter, D. The Thermal Transformation from Lanthanum Hydroxide to Lanthanum Hydroxide Oxide. *Thermochim. Acta* **2006**, *445* (2), 200–204.

(61) Liu, L.; Zhang, C.; Wang, W.; Li, G.; Zhu, B. Decomposition of SO2 on Ni (111) Surface and the Effect of Metal Doping: A First-Principles Study. *Molecules* **2023**, *28* (18), 6739.

(62) Mohsenzadeh, A.; Bolton, K.; Richards, T. DFT Study of the Adsorption and Dissociation

of Water on Ni (111), Ni (110) and Ni (100) Surfaces. *Surf. Sci.* **2014**, *627*, 1–10.

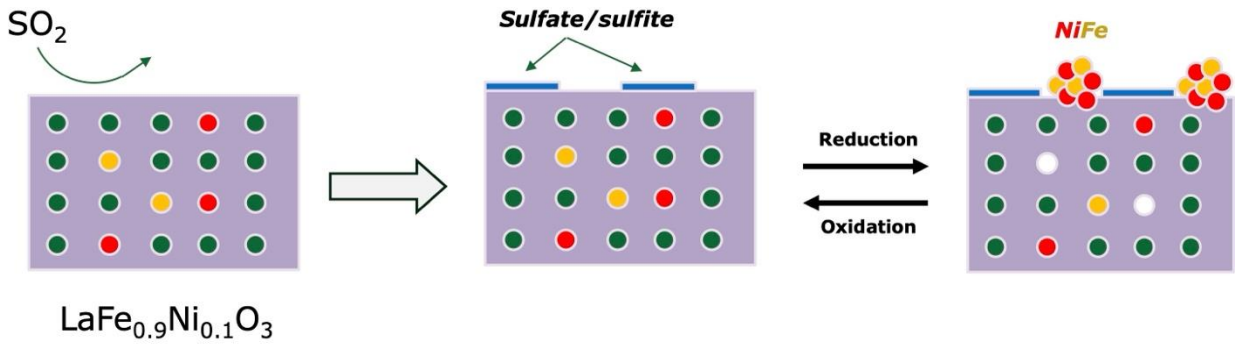
SO2
Sulfate/sulfite
NiFe
Reduction
Oxidation
LaFe0.9Ni0.1O3

Supporting Information

Influence of SO_2 on NiFe Nanoparticle Exsolution and Dissolution from $LaFe_{0.9}Ni_{0.1}O_3$ Perovskite Oxides

Musa Najimu[a,b] , Matthew J. Hurlock[c] , Sahanaz Parvin[d] , Courtney Brea[i], Neelesh Kumar[e],

Yoon Jin Cho[j] , Yiqing Wu Gao[f], Guoxiang Hu[i], Zili Wu[f,g], Eranda Nikolla[j] , Jonas Baltrusaitis[d],

Tina M. Nenoff[h], Israel E. Wachs[e], Kandis Leslie Gilliard-AbdulAziz[a,b]*

a. Department of Civil and Environmental Engineering, University of Southern California, Los Angeles, California 90089, United States
b. Department of Chemical and Environmental Engineering, University of California−Riverside, Riverside, California 92521, United States
c. Materials & Systems Design, Pacific Northwest National Laboratory, Richland, Washington 99345, United States
d. Department of Chemical and Biomolecular Engineering, Lehigh University, Bethlehem, Pennsylvania 18015, United States
e. Operando Molecular Spectroscopy and Catalysis Laboratory, Department of Chemical and Biomolecular Engineering, Lehigh University, Bethlehem, Pennsylvania 18015, United States
f. Chemical Sciences Division, Oak Ridge National Laboratory, Oak Ridge, Tennessee 37831, United States
g. Center for Nanophase Materials Sciences, Oak Ridge National Laboratory, Oak Ridge, Tennessee 37830, United States
h. Advanced Science and Technology, Sandia National Laboratories, Albuquerque, New Mexico 87185, United States
i. School of Materials Science and Engineering, College of Engineering, Georgia Institute of Technology, Atlanta, GA 30332, United States
j. Department of Chemical Engineering, University of Michigan, Ann Arbor, Michigan 48109, United States

Corresponding Author

*To whom all correspondence should be addressed. Telephone: (213) 821-2169
E-mail address: kabdulaz@usc.edu

Table of Contents

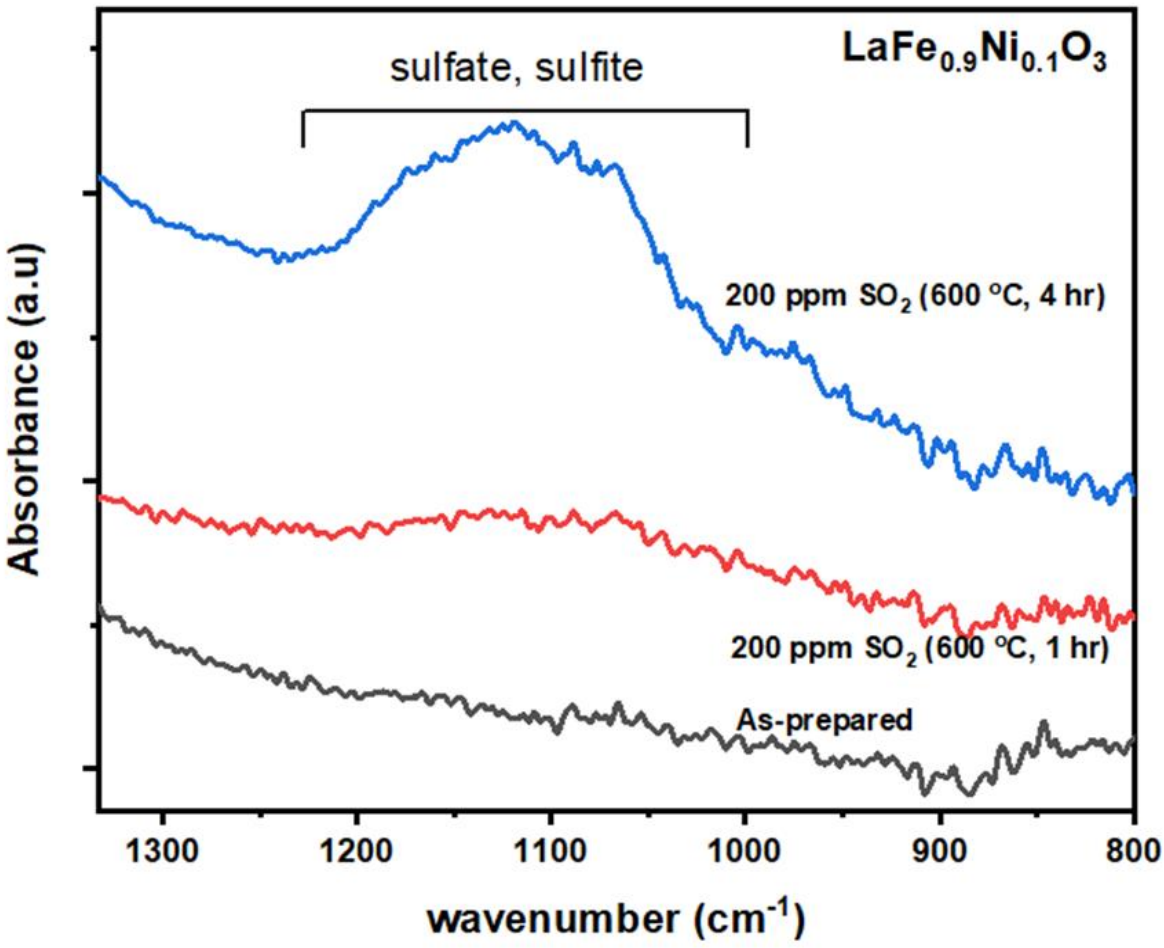

Figure S1: FTIR spectra of as-prepared $LaFe_{0.9}Ni_{0.1}O_3$ and dry SO_2-exposed $LaFe_{0.9}Ni_{0.1}O_3$ after 1 h and 4 h exposure [200 ppm SO_2 at 600°C]

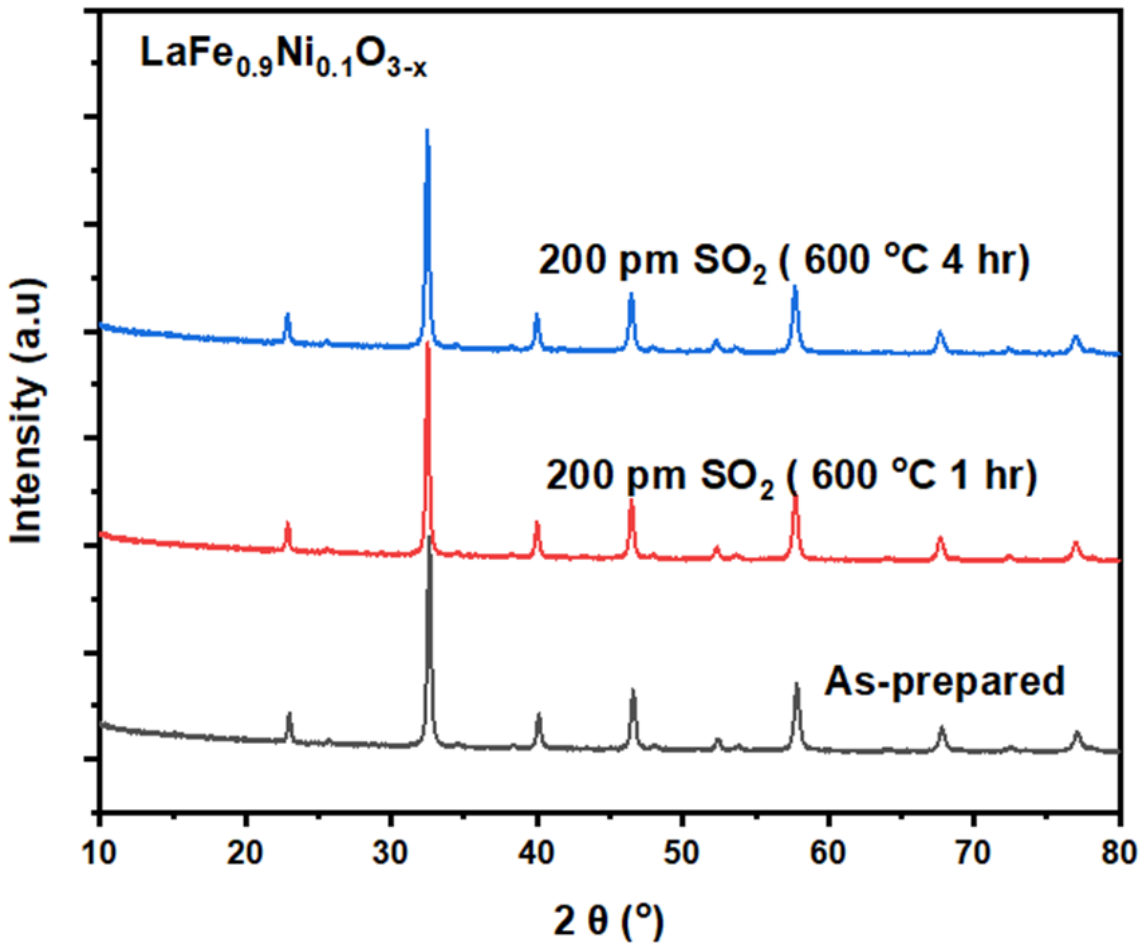

Figure S2: XRD patterns of as-prepared $LaFe_{0.9}Ni_{0.1}O_3$ and dry SO_2-exposed $LaFe_{0.9}Ni_{0.1}O_3$ after 1 h and 4 h exposure [200 ppm SO_2 at 600^oC]

(a)

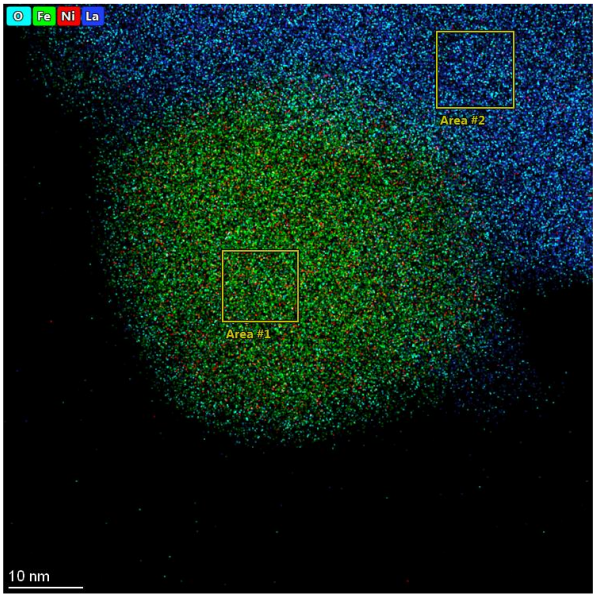

(b)

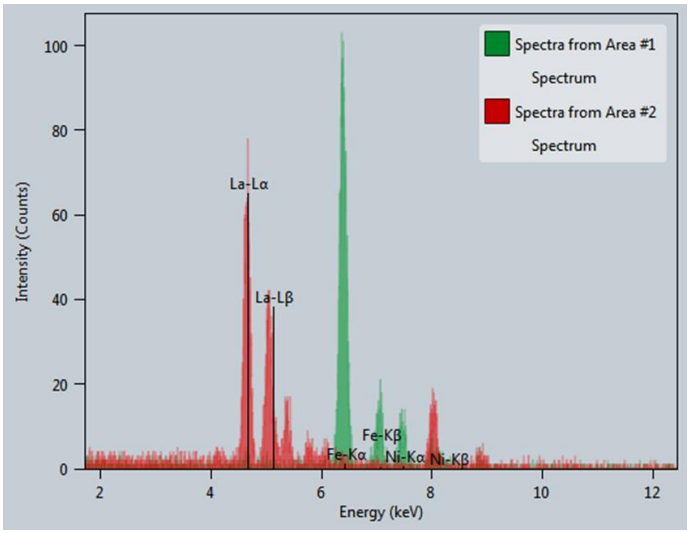

Figure S3(a) STEM-EDS image of an enclosed nanoparticle of reduced as-prepared $LaFe_{0.9}Ni_{0.1}O_3$ (b) EDS intensity profile of an area in exsolved nanoparticle and perovskite oxide region – The intensity of Fe is higher in area 1 (exsolved nanoparticle region) than in area 2 (perovskite oxide area)

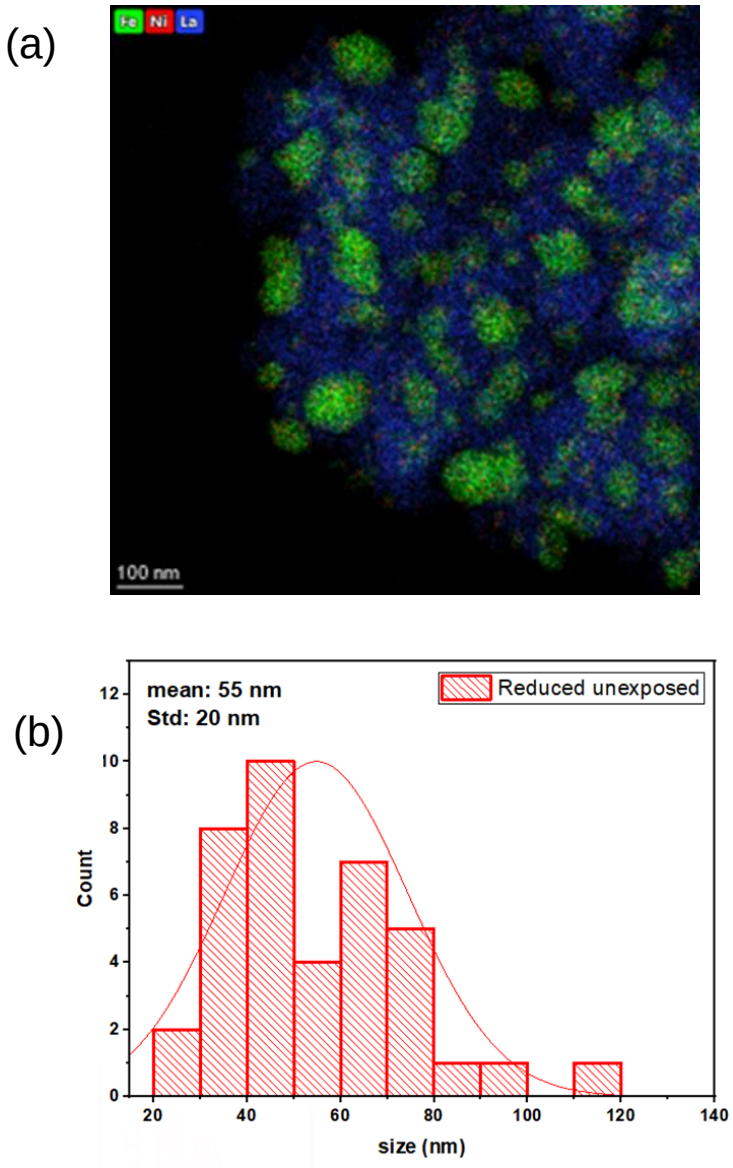

Figure S4: (a) STEM-EDS image of exsolved nanoparticles after reduction of as-prepared $LaFe_{0.9}Ni_{0.1}O_3$ (b) Particle size distribution of exsolved NiFe nanoparticles after reduction of as-prepared $LaFe_{0.9}Ni_{0.1}O_3$ (Reduction: 5% H_2/He 800^{o}C for 2 h, oxidation: 20% O_2/He 800^{o}C for 2 h)

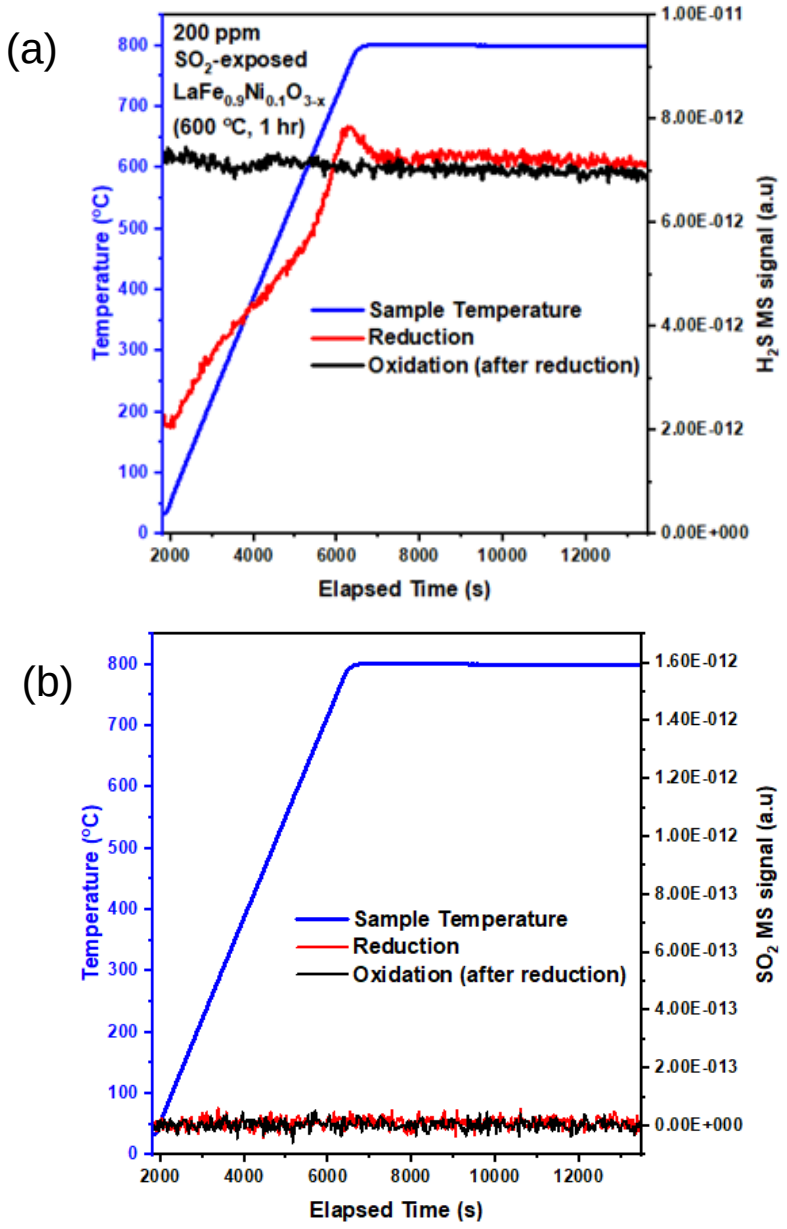

Figure S5: (a) H_2S tracking during first reduction and subsequent oxidation stage of SO_2-exposed LFNO (b) SO_2 tracking during first reduction and subsequent oxidation stages of SO_2-exposed LFNO - Reduction: 5% H_2/He 800°C for 2 h, oxidation: 20% O_2/He 800°C for 2 h

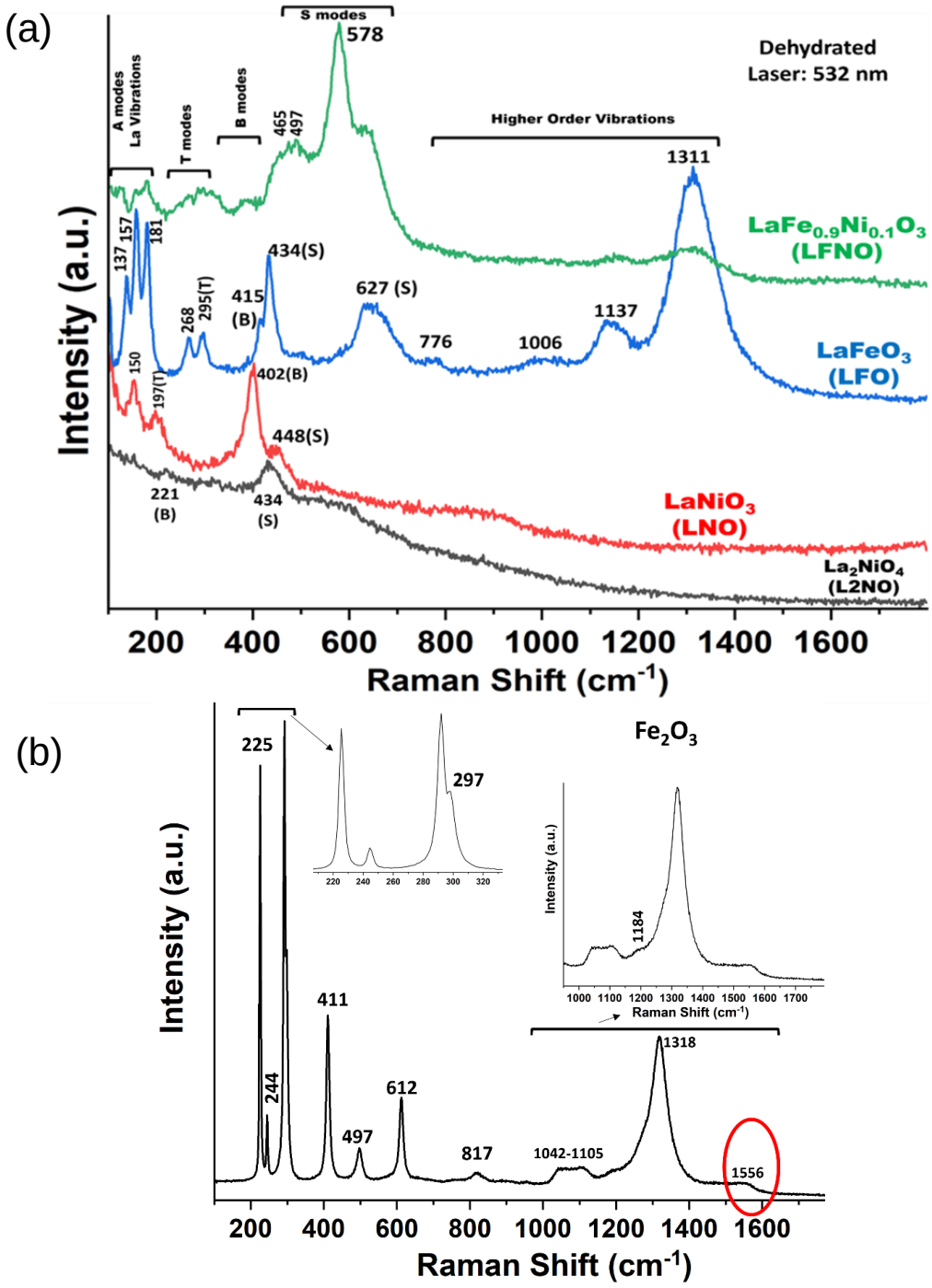

Figure S6: Raman spectra of (a) dehydrated $LaFe_{0.9}Ni_{0.1}O_3$, $LaFeO_3$, and $LaNiO_3$ using 532 nm laser excitation (b) dehydrated iron oxide.

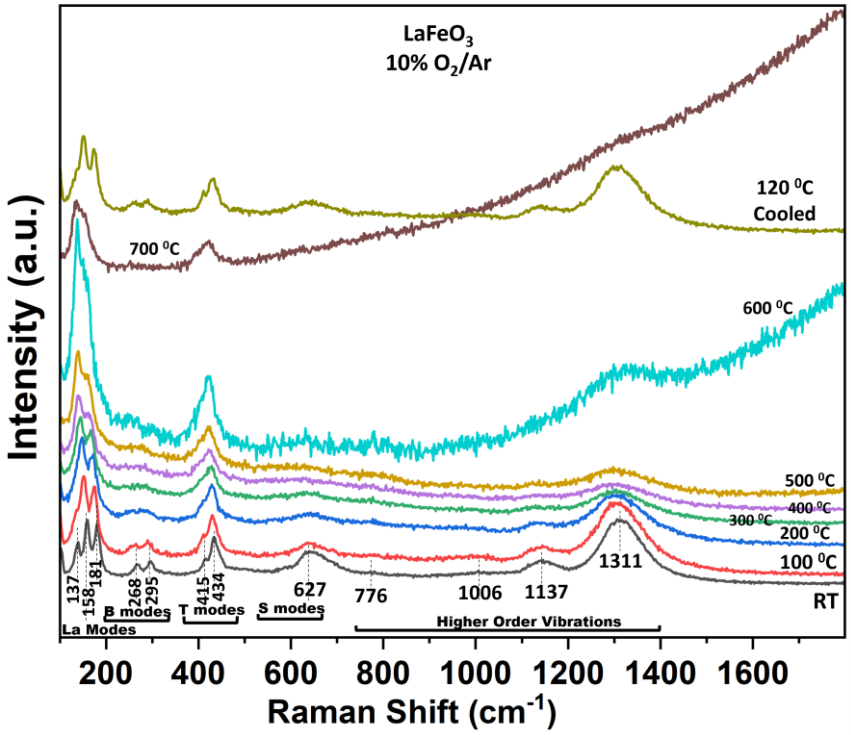

Figure S7 (a) Raman spectra of $LaFeO_3$ under 10% O_2/Ar with increasing temperature and after cooling

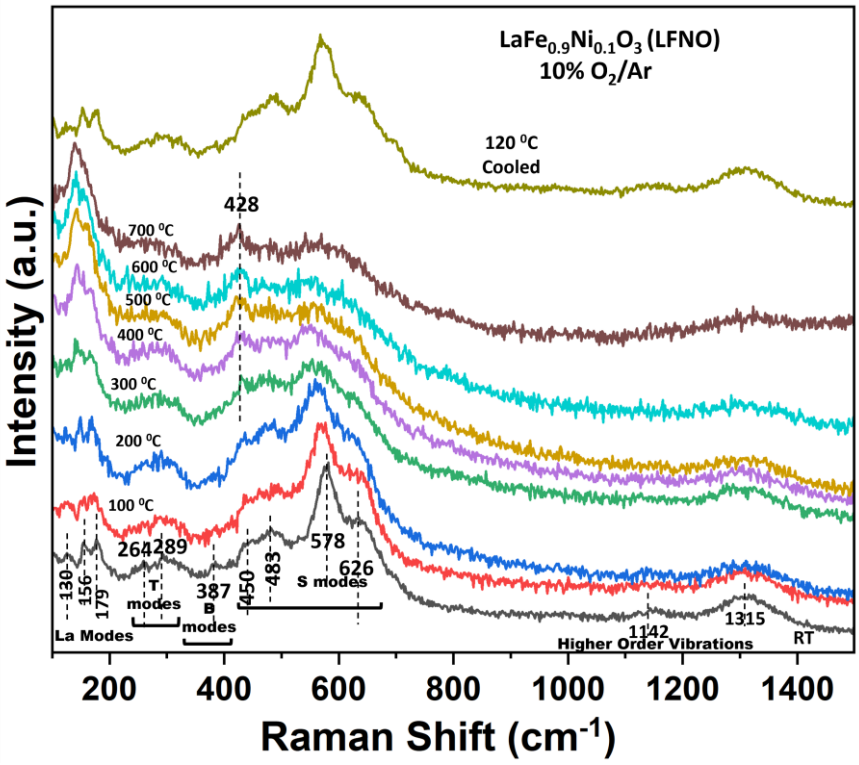

Figure S8 (a) Raman spectra of LFNO under 10% O_2/Ar with increasing temperature and after cooling

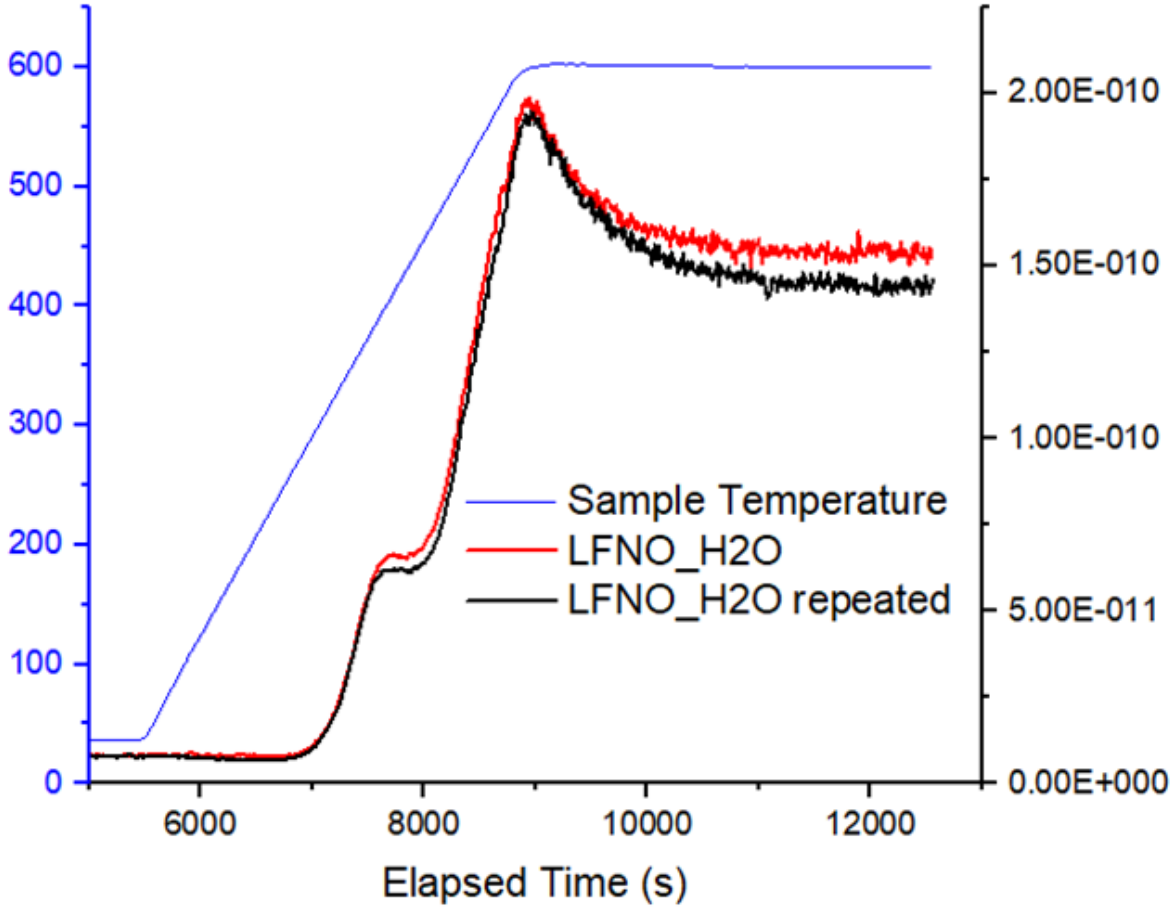

Figure S9: Thermochemical water splitting performance (H_2 MS signal) of two different samples of as-prepared LFNO [Water exposure: 5% H_2O/He, temperature ramping to 600^oC at 10^oC/min and dwelling at 600^oC for 1 h]

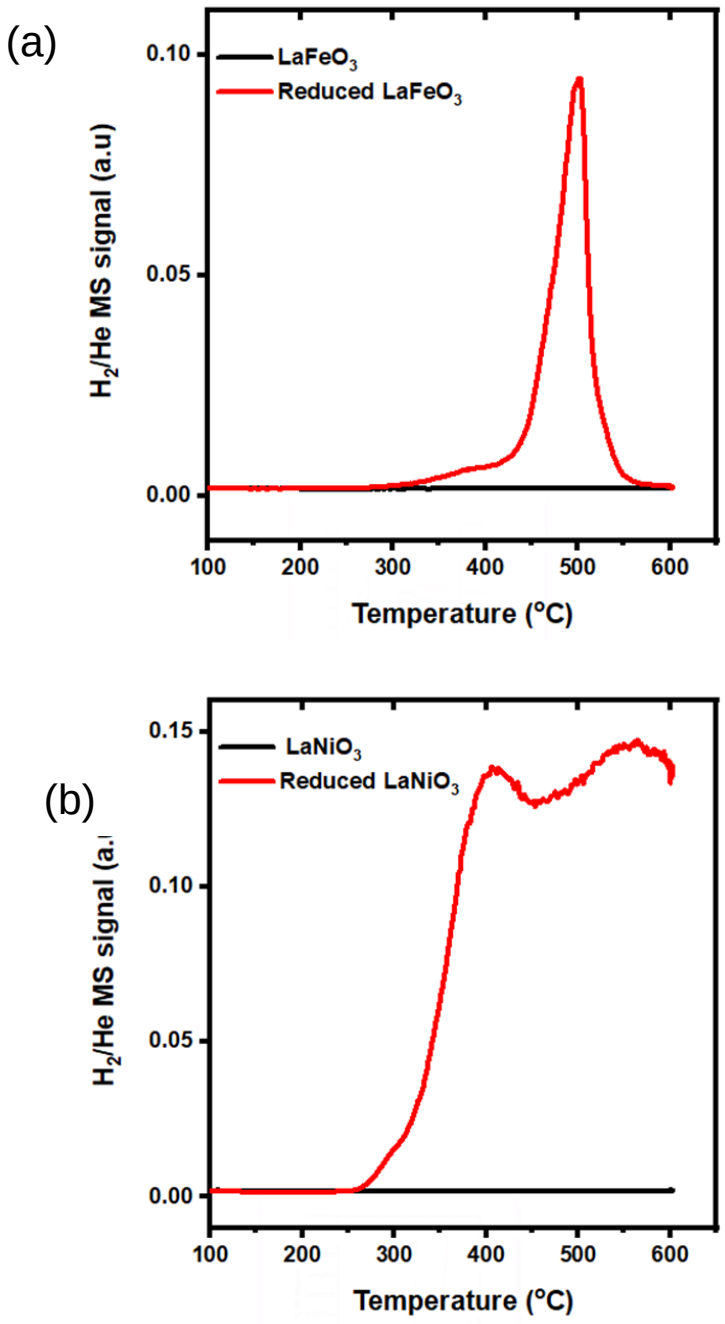

Figure S10: Normalized H_2 MS signal from thermochemical water splitting performance of (a) as-prepared and reduced $LaFeO_3$ (c) as-prepared and reduced $LaNiO_3$ [Water exposure: 5% H_2O/He, temperature ramping to 600^oC at 10^oC/min and dwelling at 600^oC for 1 h, reduction: 5% H_2/He 800^oC for 2 h, oxidation: 20% O_2/He 800^oC for 2 h]

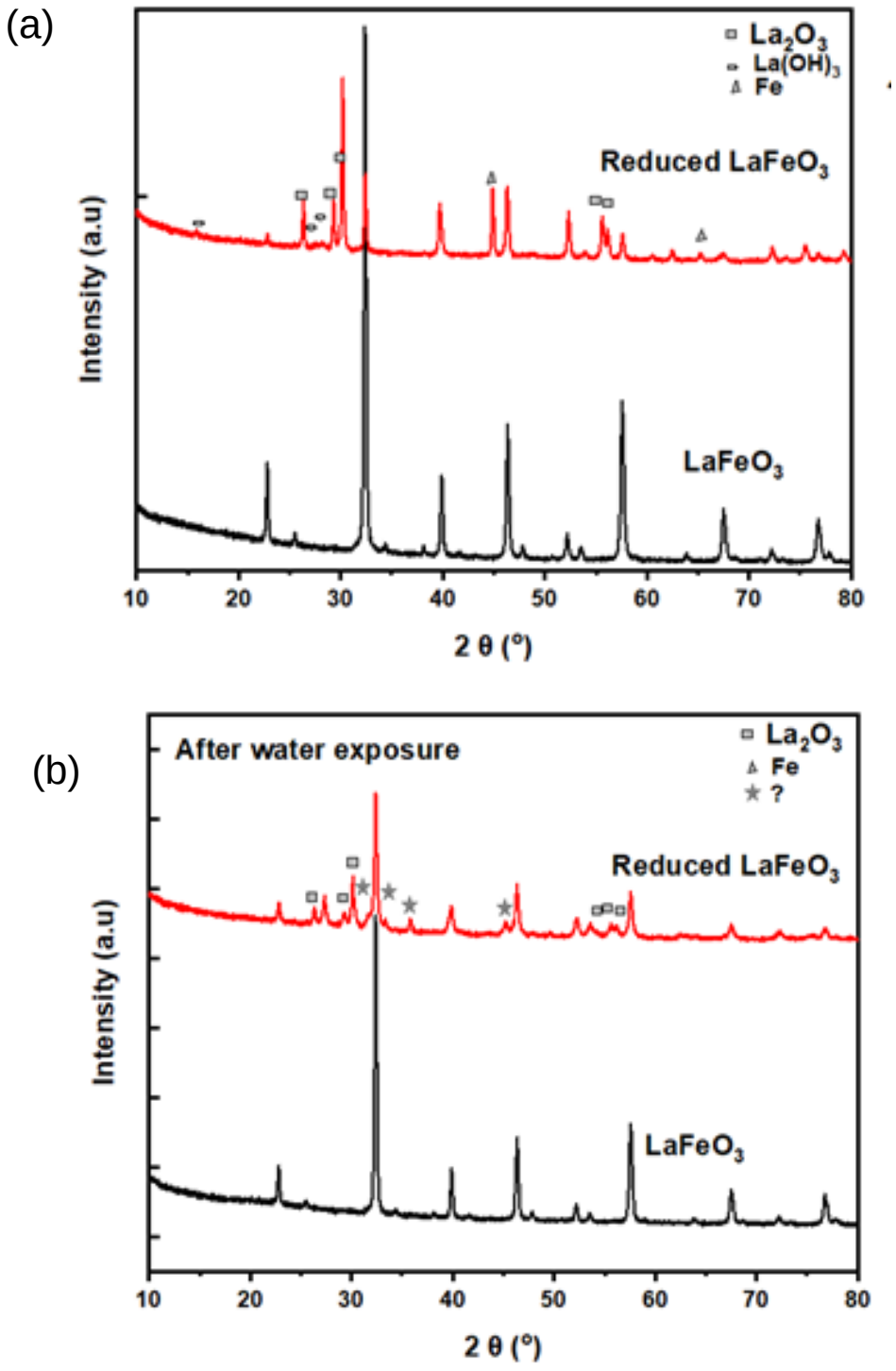

Figure S11: XRD patterns of as-prepared and reduced $LaFeO_3$ perovskite oxide (a) before and (b) after water exposure [Water exposure: 5% H_2O/He, temperature ramping to 600^oC at 10^oC/min and dwelling at 600^oC for 1 h]

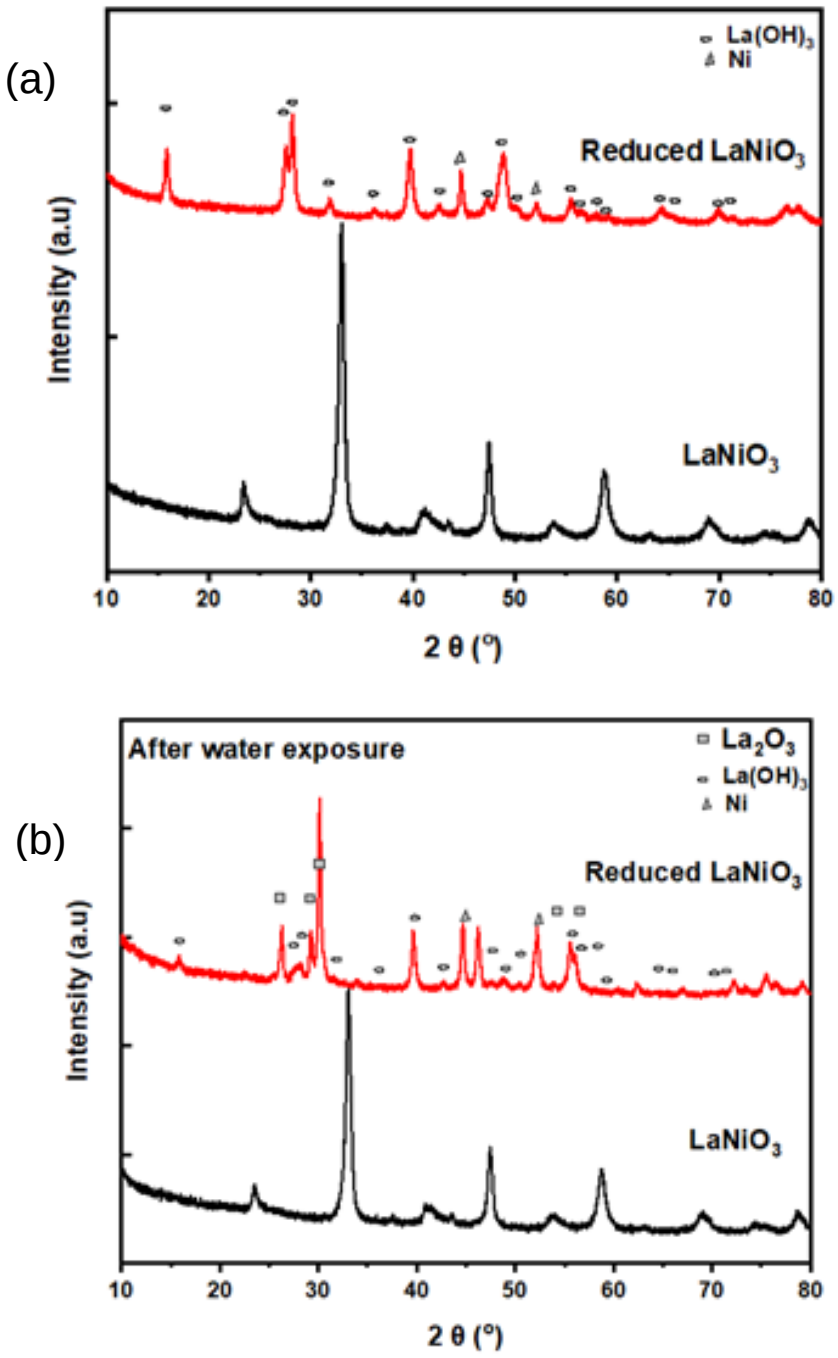

Figure S12: XRD patterns of as-prepared and reduced $LaNiO_3$ perovskite oxide (a) before and (b) after water exposure [Water exposure: 5% H_2O/He, temperature ramping to 600°C at 10°C/min and dwelling at 600°C for 1 h].

The observed $La(OH)_3$ in ex-situ XRD of reduced $LaNiO_3$ could have been due to hydration of La_2O_3 by the atmospheric moisture [1].

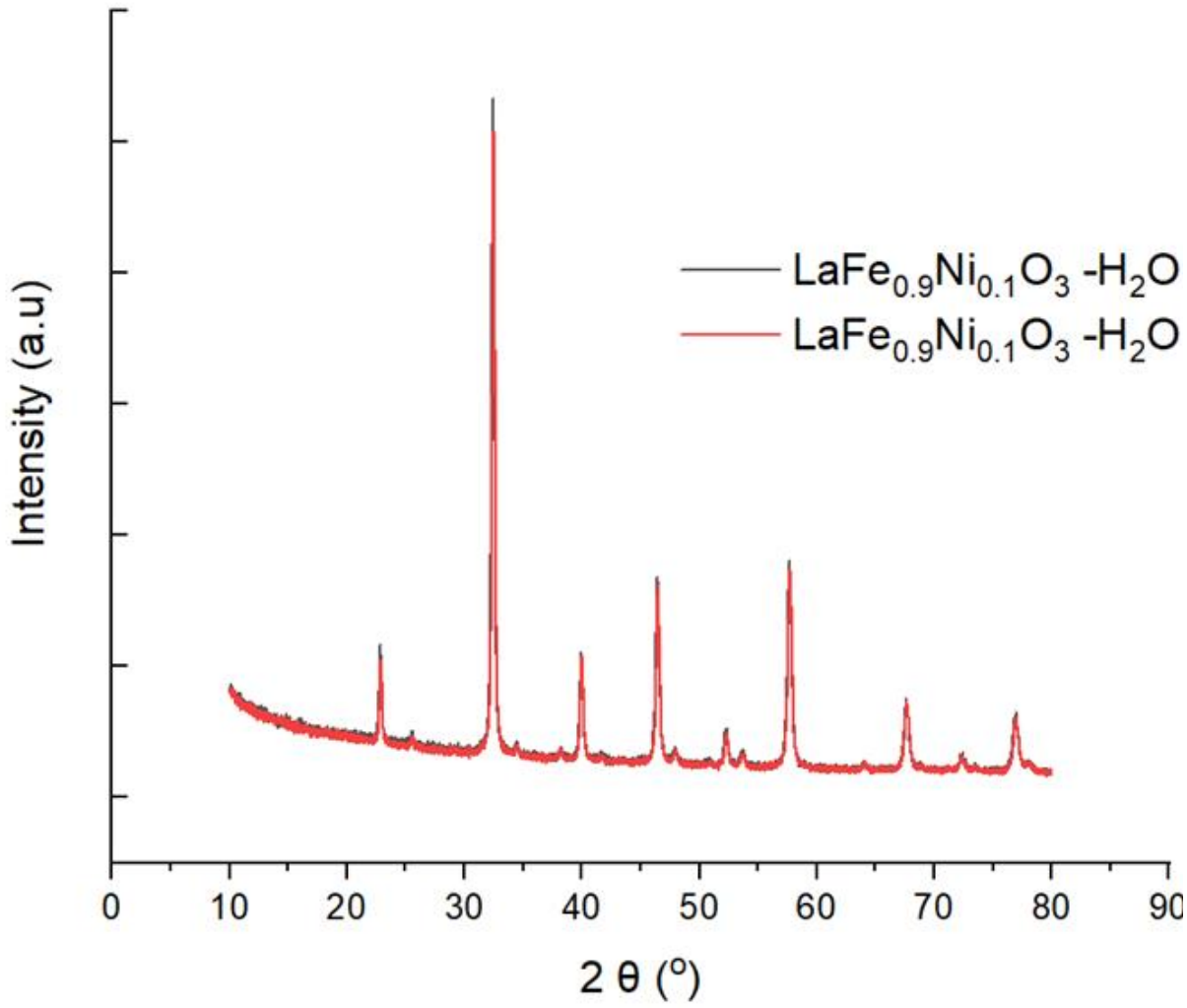

Figure S13: XRD patterns of two as-prepared LFNO samples after water exposure [Water exposure: 5% H_2O/He, temperature ramping to 600°C at 10°C/min and dwelling at 600°C for 1 h]

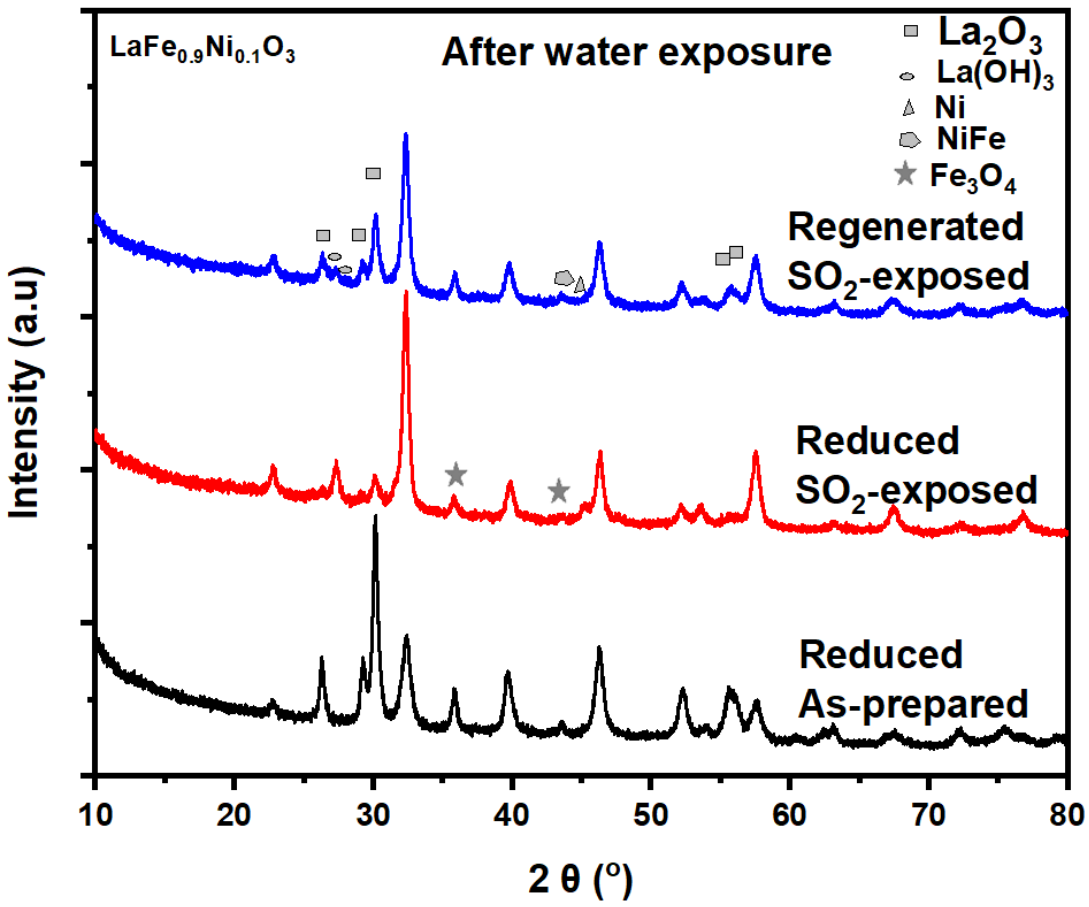

Figure S14: XRD of reduced as-prepared, reduced SO_2-exposed and regenerated SO_2-exposed $LaFe_{0.9}Ni_{0.1}O_3$ perovskite oxide, after water exposure, [Water exposure: 5% H_2O/He, temperature ramping to 600^oC at 10^oC/min and dwelling at 600^oC for 1 h, reduction: 5% H_2/He 800^oC for 2 h, oxidation: 20% O_2/He 800^oC for 2 h]

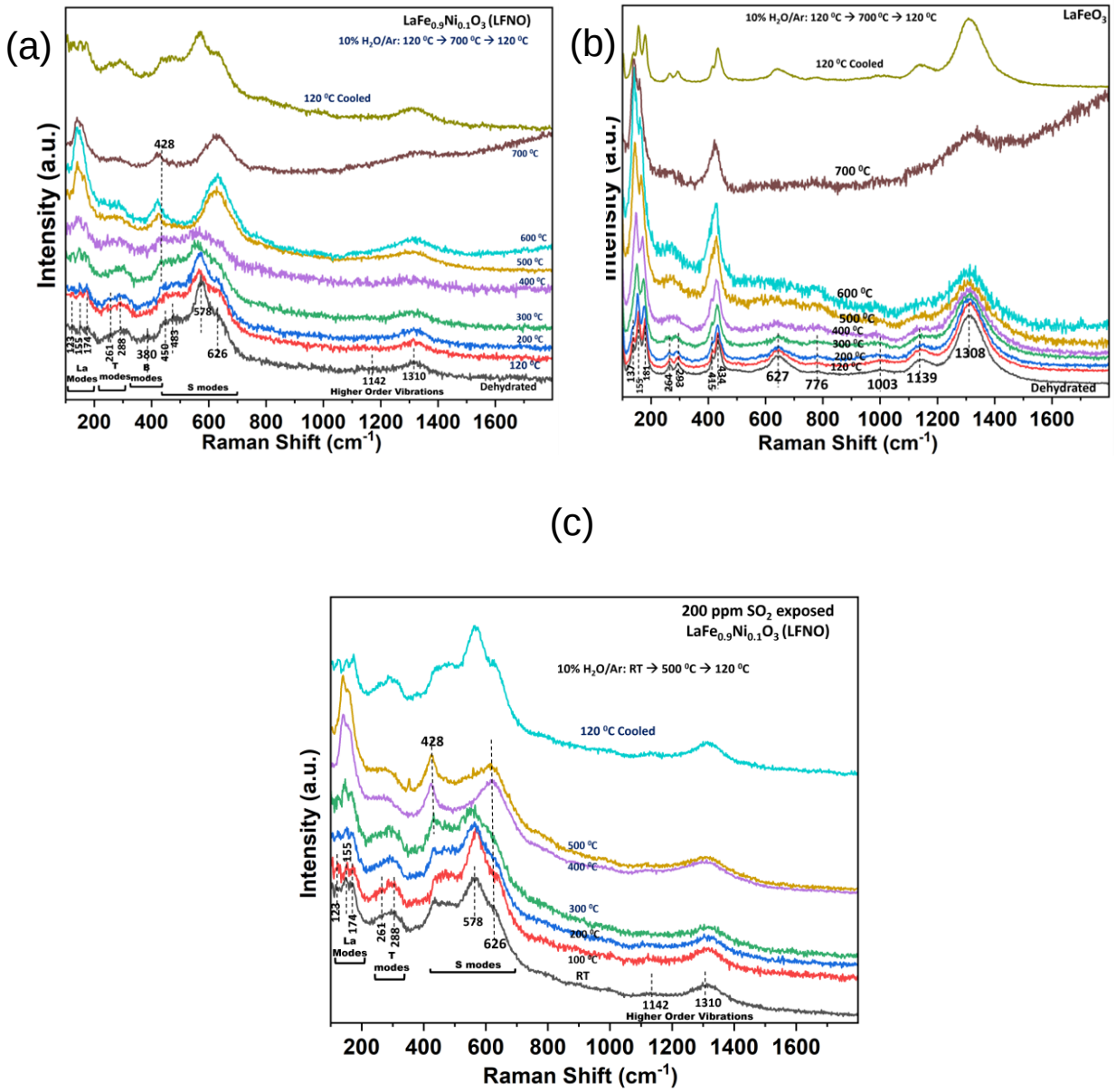

Figure S15: In Situ Raman spectra for (a) LFNO, (b) LFO, and (c) SO_2-exposed LFNO collected under 10% H_2O/Ar with increasing temperature and subsequent cooling to 120°C

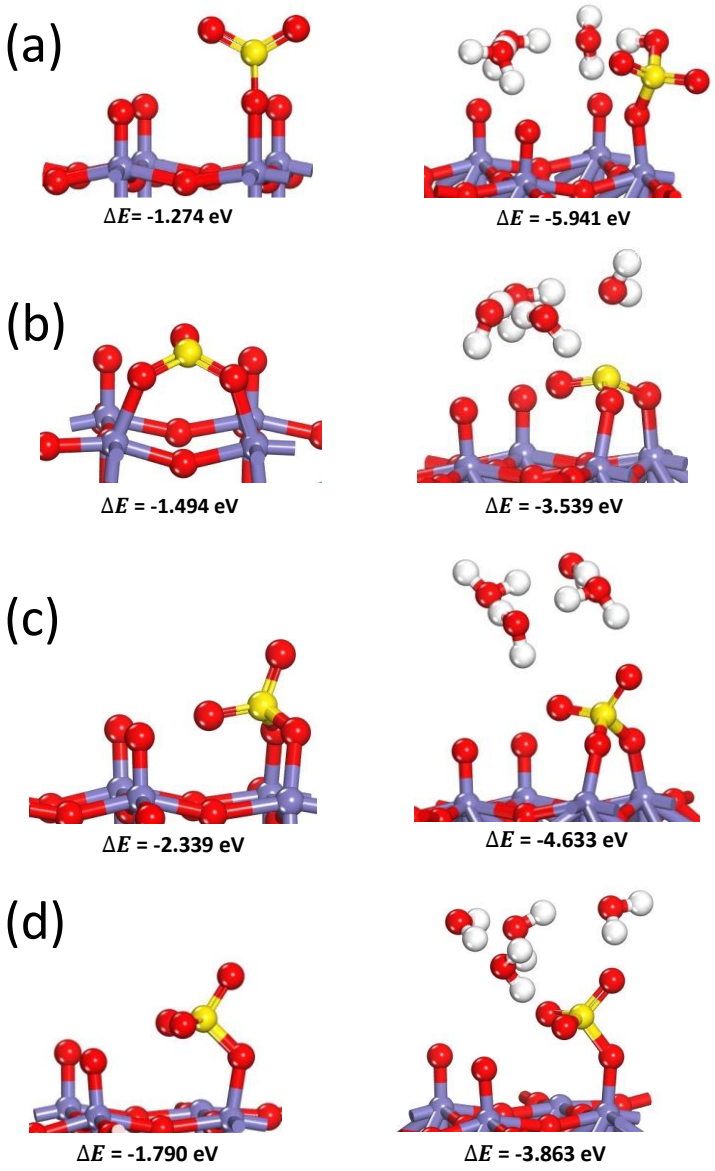

Figure S16. Optimized geometries of (de)hydrated (a) monodentate sulfite and bisulfate (b) bidentate sulfite (c) bidentate sulfate and (d) monodentate sulfate species at LFO. Fe, light purple; O, red; H, white; S, yellow.

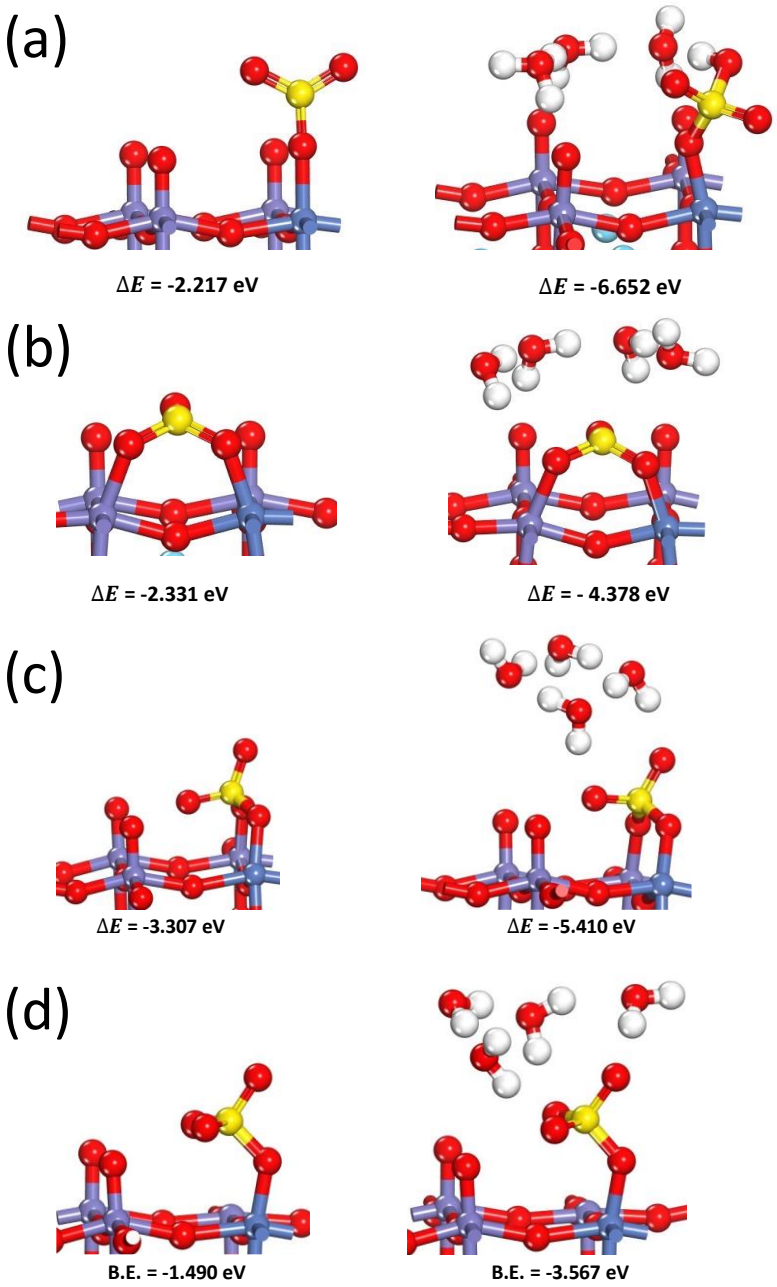

Figure S17. Optimized geometries of (de)hydrated (a) monodentate sulfite and bisulfate (b) bidentate sulfite (c) bidentate sulfate and (d) monodentate sulfate species at Ni-doped LFNO. Fe light purple; O, red; H, white; S, yellow.

Table S1. DFT calculated vibrational frequencies for (de)hydrated sulfur species on LFNO and LFO

Sulfur Species	**LFNO**		**LFO**	
	Hydrated (cm^{-1})	Dehydrated (cm^{-1})	Hydrated (cm^{-1})	Dehydrated (cm^{-1})
Bidentate sulfate	1066.39 1200.01	1067.76 1200.29	1070.79 1217.32	1078.76 1237.51
Monodentate sulfate	950.24 1008.25 1029.09	960.71 1003.66 1020.32	971.12 1081.07 1099.80	976.15 1038.75 1061.79
Bidentate sulfite	939.67 1166.60	954.62 1164.92	834.04 1145.90	847.29 1145.68
Bisulfate	1101.16 1240.67 1292.83		1112.90 1266.41 1321.59	
Monodentate sulfite		995.26 1297.69		998.22 1289.58

References

[1] A. Singh, V. Palakollu, A. Pandey, S. Kanvah, and S. Sharma, “Green synthesis of 1, 4-benzodiazepines over La_2O_3 and $La(OH)_3$ catalysts: Possibility of Langmuir–Hinshelwood adsorption,” *RSC Adv.*, vol. 6, no. 105, pp. 103455–103462, 2016.